




# A multiscale constitutive model for the elasticity of clay nanoparticle assemblies

Hejian Zhu<sup>a,b,c</sup> \*, Andrew J. Whittle<sup>c</sup>, Roland J.-M. Pellenq<sup>d,e</sup>

<sup>a</sup> Department of Aerospace Engineering, Texas A&M University, 710 Ross St, College Station, 77843, TX, USA

<sup>b</sup> School of Civil and Environmental Engineering, Georgia Institute of Technology, 790 Atlantic Dr NW, Atlanta, 30332, GA, USA

<sup>c</sup> Department of Civil and Environmental Engineering, Massachusetts Institute of Technology, 77 Massachusetts Ave, Cambridge, 02139, MA, USA

<sup>d</sup> EpiDaPo Lab-CNRS/George Washington University, USA

<sup>e</sup> European Institute of Membranes, Centre National de la Recherche Scientifique, 300 Av. du Professeur Emile Jeanbrau, Montpellier, 34090, France

## ARTICLE INFO

### Keywords:

Multiscale  
Constitutive model  
Clay  
Elasticity

## ABSTRACT

Due to its particulate nature, the mechanical properties of bulk clay are determined by interparticle forces and fabrics of particle assemblies. A thorough study of the connection between properties across length scales is crucial to a fundamental understanding of the mechanisms behind the complex mechanical behavior of clays and clayey soils. This paper demonstrates the development of a multiscale constitutive model for describing the small-strain elastic properties of illite, based on the results of coarse-grained mesoscale molecular dynamic simulations for monodisperse assemblies of illite primary particles. The formulation consists of a homogenization scheme linking the potential energy of the system with an optimal parameter set describing the mesoscale fabric of the particles, and a perturbation scheme describing the change of the parameters in response to infinitesimal strains applied to the systems. The small strain elastic stiffness tensors are calculated as the second-order derivative of the potential energy with respect to the infinitesimal strain. The results from model prediction are validated against the stiffness properties interpreted from numerical simulations as well as experimental findings from prior research studies. The multiscale constitutive model is able to effectively capture the elastic properties of illite in terms of magnitude and material symmetry purely based on the information of interparticle forces and fabrics.

## 1. Introduction

The mechanical properties of clays are greatly affected by the surface chemistry and crystalline nature of their primary particles and the microscopic structures of the particle assemblies (Mitchell and Soga, 2005), which limits the capabilities of soil models to capture the underlying mechanisms. In order to develop more reliable predictions of clay behavior, a multiscale modeling framework should be considered.

In general, there are two possible directions for multiscale modeling: top-down and bottom-up. Top-down approaches incorporate multiphysical features into conventional (macroscopic continuum) soil model, through establishing thermo–hydro–chemo–mechanical (THCM) coupled formulations. The models are developed either through incorporating empirical models in the conventional soil parameters, or through thermodynamic analysis (e.g. Coussy, 2003, 2007) based on postulates originating from experimental

\* Corresponding author.

E-mail address: [pzh@tamu.edu](mailto:pzh@tamu.edu) (H. Zhu).

<https://doi.org/10.1016/j.jmps.2025.106140>

Received 6 August 2024; Received in revised form 27 February 2025; Accepted 1 April 2025

Available online 17 April 2025

0022-5096/© 2025 Elsevier Ltd. All rights are reserved, including those for text and data mining, AI training, and similar technologies.

observations at a lower length scale. Early attempts are exemplified by Gens and Alonso (1992) for unsaturated expansive clays. Thermodynamically consistent formulations include (Hueckel, 1992; Heidug and Wong, 1996; Hueckel, 2005). However, obtaining the parameters of these models requires complex experimental investigations, while the models themselves are usually based on rather simplified postulates, such that the micro- and mesoscale mechanisms are not fully revealed.

Bottom-up approaches, on the other hand, proceed from simulations at lower length scales. Depending on the nature of the materials, researchers may choose different types of bottom-up multiscale modeling schemes. Existing schemes are customarily classified into two categories, sequential and concurrent methods (Gooneie et al., 2017; Horstemeyer, 2009). In sequential methods, the information is transferred bottom-up through series of coarse-graining techniques, i.e., the information obtained through simulation at a smaller length scale is condensed into a smaller set of parameters/variables and used in the simulation at a larger length scale. These methods are more suitable for systems where phenomena at different length scales are weakly coupled. The core of these methods is to select the appropriate coarse-graining methods that save computational cost and optimize the transfer of essential information. Concurrent methods typically group only some units through coarse-graining so that the resulting systems contain constituting units with different length scales. These methods are suitable for systems where the collective behavior is dominated by interactions between constituents across different length scales. The difficulty therefore lies in the interface and interaction between elements of different length scales.

In the field of porous media, there are multiple types of materials exhibiting multiscale features. In the bottom up study of granular materials, there have been extensive research efforts to develop the appropriate micromechanical definitions of the common macroscopic quantities, including stress, strain, shear strength, etc, which corresponds to a homogenization approach. The definitions can vary and may not be consistent among researchers. Notable prior studies include (Bagi, 2006; Christoffersen et al., 1981; Kruyt and Rothenburg, 2004; Zhu and Yu, 2002; Chen, 2019; NejadSadeghi and Misra, 2020), that provide theoretical support for coupled simulation methods, in the form of discretized extended formulations of the continuum mechanical theories, enabling the transfer of information from simulation at a lower length scale to be used in macroscale simulations. The actual realization of the formulation varies, as exemplified in the studies including (Andrade et al., 2011; Karapiperis et al., 2021; Mital and Andrade, 2022). One of the major purposes behind these studies is to introduce the internal length scales and mechanisms related to the special properties of granular material such as the formation of shear bands and particle segregation in granular flow. The internal length scales were traditionally introduced in continuum models in the form of strain-gradient theories (e.g., Kuhn, 2005; Placidi et al., 2021). There are also models capturing microscopic mechanisms through mathematical devices representing slip systems (Gu et al., 2001), and friction-inertial relations (Baumgarten and Kamrin, 2019; Kamrin, 2017, 2018).

In the case of clay materials, sedimentation and consolidation certainly involve large deformations while swelling behavior of some clay minerals due to hydration of particles (i.e., crystalline swelling) is not readily described at the continuum level. Therefore powerful constitutive models are crucial to engineering design practice. Microscopically, the most commonly-occurring clay minerals comprise thin plate-shaped monoclinic crystals with thickness  $\sim 1$  nm and diameter/thickness of  $10^2$  to  $10^4$ :1 (Mitchell and Soga, 2005). Research studies have been carried out investigating the mean interactions between primary particles during hydration process (Carrier, 2014; Ebrahimi et al., 2012, 2014; Brochard et al., 2012, 2017; Brochard, 2021; Honorio et al., 2017; Holmboe et al., 2012; Zhu et al., 2022, 2025), based on which interpretations of the elastic properties have also been provided and compared to experimental results. Ebrahimi et al. (2014) developed a multiscale simulation scheme that involves coarse-graining technique from nanoscale to mesoscale simulations, which forms the basis of this research study. Recently, Asadi et al. (2022) have proposed a novel mesoscale force field that can simulate the hysteretic behavior during hydration–dehydration process. While nano- and mesoscale simulations greatly improve our understanding of the microstructures and properties of clay materials, there are as yet no multiscale constitutive models for clays based on this information. The behaviors are more commonly simulated with heuristic models in current engineering practice.

Here, we adopt a sequential modeling scheme based on the simulation methods proposed by Ebrahimi et al. (2014) involving studies at three length scales: nano-, meso- and macroscales. At nanoscale, the interactions between illite and smectite primary particles were studied using a free energy perturbation method (Zhu et al., 2022). The information was used to fit a coarse-grained force field in the form of a Gay–Berne potential (Everaers and Ejtehadi, 2003; Gay and Berne, 1981), which was used in mesoscale molecular dynamics simulations to study the mechanical properties (hydrostatic compression and small-strain shear behaviors) of an assemblies of particles in relation to the fabrics of the particles (Zhu et al., 2025). The results were used to generate a set of parameters to characterize the particle assemblies. This paper presents the establishment of a constitutive model describing the elastic properties of clay minerals based on the observations of mesoscale simulations through theoretical derivations building on the interparticle forces and fabric information. Section 2 briefly reviews the background modeling at the nano and mesoscale which forms the basis of the model developed in this work. It also summarizes the parameters used in the derivation of the model including the parameters describing the mesoscale fabric of the clay particle assemblies, and the parameters in the interaction model between pairs of particles. Section 3 presents the derivation and validation of the constitutive model, including the homogenization scheme and the perturbation scheme respectively. Section 4 summarizes the findings and discuss about possible further development of the work.

The multiscale constitutive model is able to effectively capture the elastic properties of illite in terms of magnitude and material symmetry purely based on the information of interparticle forces and fabrics. It forms the basis of further development of a multiscale elasto-plastic model. The application scenarios go beyond the systems presented in the paper and the methodology has broader significance in the opening up a new upscaling approach for geomaterials and engineering materials in general.

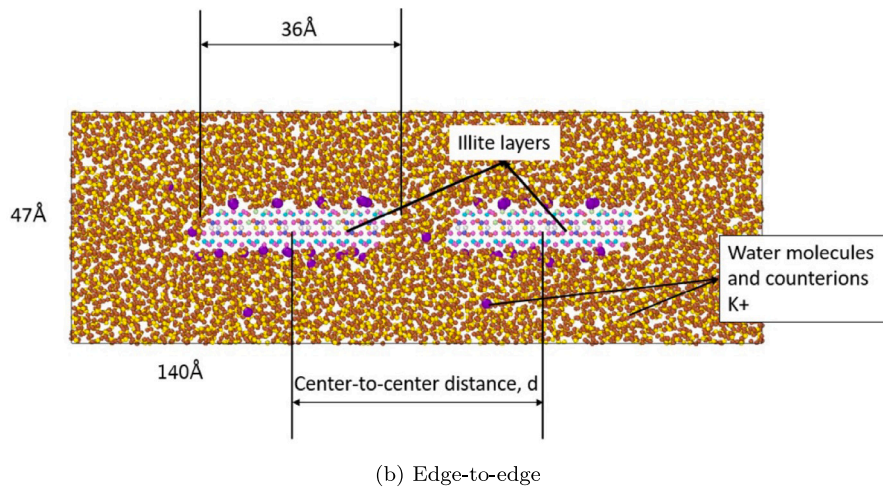
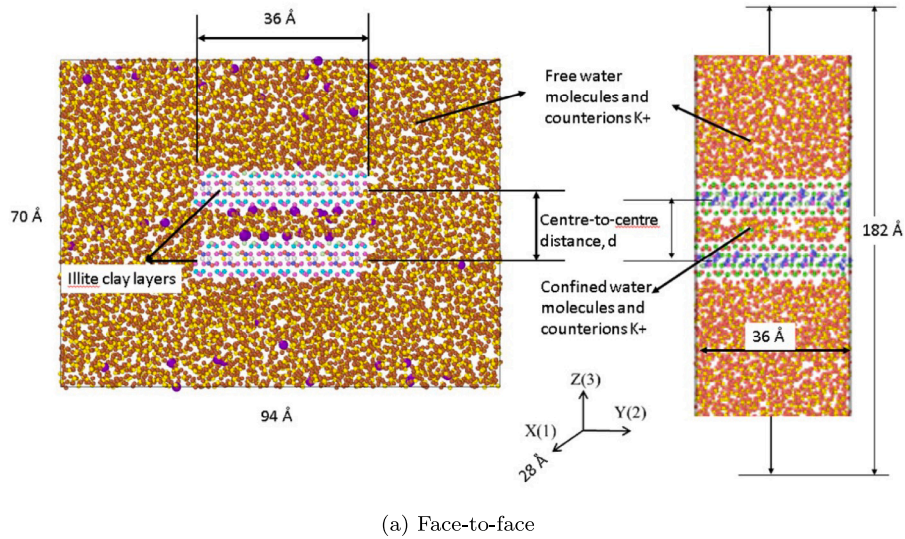


Fig. 1. Configuration for the free energy perturbation at the nanoscale for the potential of mean force interactions between the illite nanoparticles.

## 2. Prior works and model parameters

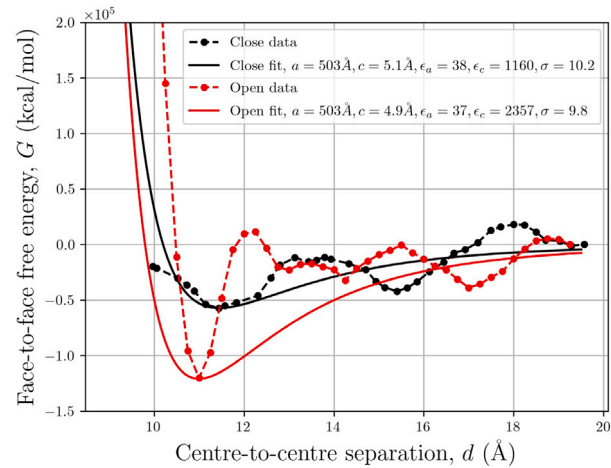
### 2.1. Summary of prior works at nano- and meso-scales

In prior works by the Authors (Zhu et al., 2022, 2025), nanoscale fully atomistic free energy perturbation calculations were carried out to study the interactions between primary 2:1 clay particles, which were then used to fit for the parameters in coarse-grained Gay–Berne force field applied in mesoscale simulations to study the aggregation and mechanical behaviors of assemblies of 1000 primary particles (represented as rigid ellipsoids) in hydrostatic compression (at four pressure levels, 1, 5, 25, and 125 atm) and small-strain shear loading conditions (Zhu et al., 2025). These modeling efforts have generated two key outcomes:

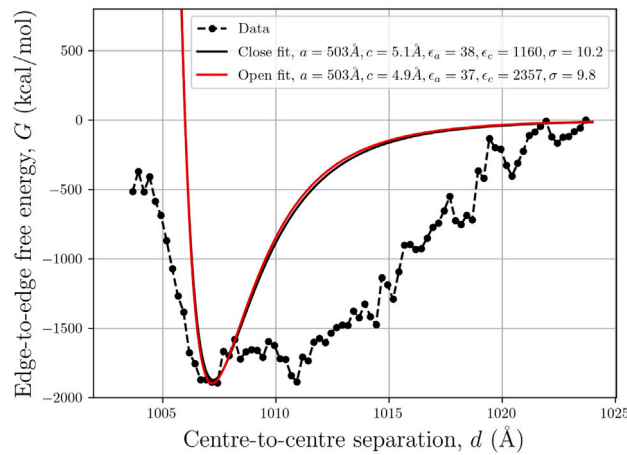
- Establishment of a set of quantitative measures to effectively describe the fabrics/mesostructures of the mesoscale assemblies of primary particles;
- Quantitative calculation of these parameters for equilibrated systems under various loading conditions.

This section briefly review the simulation setup and key results that are most relevant to the development of the constitutive model.

At the nanoscale, we initially simulate the face-to-face and edge-to-edge interactions (Fig. 1) between pairs of illite particles through full atomistic simulations (Zhu et al., 2022). Illite is a key type of 2:1 clay mineral, of which the particles are formed from an octahedral alumina layer between two tetrahedral silicate layers combined through sharing oxygen atoms. The nanoparticles are negatively charged due to isomorphous substitutions where some Al and Si atoms are replaced by Mg and Al atoms. In the atomistic simulations, the particles were represented as assemblies of atoms parallel to each other, mediated by water molecules



(a) Face-to-face



(b) Edge-to-edge

**Fig. 2.** Potential of mean force interactions for a illite particles in face-to-face and edge-to-edge configurations. The data are represented by dots and dashed lines, and fitting results using Gay-Berne potential are shown as solid lines. Red lines represent fitting using data for open systems and black closed systems in the face-to-face configurations.

and counterions ( $K^+$ ). For the face-to-face interactions we also simulated two cases: (1) closed systems (infinite platelets) where there is no migration of counterions to or from the interlayer space; and (2) open systems where counterions ions are able to migrate.

The mean interactions between particles are not simply the pairwise summation of interatomic potentials, but are determined by the presence of water molecules and counterions in the interlayer space. We applied a free energy perturbation method to obtain the information. In this method, the particles were set to a series of fixed separations for relaxation, and the separation between particles were perturbed to larger and smaller separation to obtain the free energy differences due to the perturbation of separation through ensemble average of the potential energy difference brought about by the perturbation, through the following relations (Zwanzig, 1954; Chipot and Pohorille, 2017):

$$\Delta G(i \rightarrow i+1) = k_B T \ln \left[ \frac{\langle \exp(-\beta \Delta U(i \rightarrow i+1)) \rangle_i}{\langle \exp(-\beta \Delta U(i+1 \rightarrow i)) \rangle_{i+1}} \right] \quad (1)$$

where  $k_B = 1.38065 \times 10^{-23}$  J/K is the Boltzmann's constant,  $\beta = 1/(k_B T)$ ,  $T$  is the absolute temperature, and  $\langle \cdot \rangle$  is the ensemble average.

The resulting potential of mean force (PMF) curves are summarized in Fig. 2 for illite in the face-to-face and edge-to-edge configurations. The face-to-face PMFs were scaled by area and edge-to-edge by side length from the size simulated at nanoscale to represent particles with in-plane diameter of 100 nm. Both open and closed systems shown a general trend with near-field repulsive and far-field attractive interactions, together with oscillatory features corresponding to the formation of structured water layers.

The PMF curves were used to fit for a coarse-grained force field representing the interaction between rigid ellipsoids in the form of Gay–Berne (GB) potential (Eveaers and Ejtehadi, 2003; Gay and Berne, 1981), which is a function depending on the center-of-mass distance and relative orientation of the particles containing three multiplicative terms:

$$U_{\text{GB}} = u_{\text{LJ}}\eta\chi \quad (2)$$

where  $u_{\text{LJ}}$  is the Lennard-Jones (LJ) kernel, and  $\eta$  and  $\chi$  are shape and orientation-related terms. The fitting result is shown as solid lines in Fig. 2. The GB potential is not able to capture the oscillatory features, but as a first approximation, the general trend, the position and depth of the potential wells are well represented.

The most widespread formulation is for general dissimilar ellipsoids of arbitrary dimensions. The functional form of the multiplicative terms (Eveaers and Ejtehadi, 2003; Gay and Berne, 1981) are as given by Eqs. (A.2) in Appendix A. The orientations for ellipsoidal particles with arbitrary shape are best represented by quaternions. In our case, the mesoscale clay particles are represented as axisymmetric ellipsoids, with in-plane diameter  $2a = 1006 \text{ \AA}$  and thickness  $2c = 9.8 \text{ \AA}$ , and that the relative potential well depths in the principal directions also satisfy  $\epsilon_a = \epsilon_b$ . The orientation can be well represented by the unit normals  $(\mathbf{n}_1, \mathbf{n}_2)$ . Appendix A presents the reformulation of the model in terms of unit normals of the particles. The final form is given by:

$$u_{\text{LJ}} = 4\epsilon \left[ \left( \frac{\sigma}{r - \tilde{\sigma} + \sigma} \right)^{12} - \left( \frac{\sigma}{r - \tilde{\sigma} + \sigma} \right)^6 \right] \quad (3)$$

$$\tilde{\sigma} = 2a \left[ 1 + \frac{\omega_1 [(\hat{\mathbf{r}} \cdot \mathbf{n}_1)^2 + (\hat{\mathbf{r}} \cdot \mathbf{n}_2)^2] + 2\omega_1^2 (\mathbf{n}_1 \cdot \mathbf{n}_2)(\hat{\mathbf{r}} \cdot \mathbf{n}_1)(\hat{\mathbf{r}} \cdot \mathbf{n}_2)}{1 - \omega_1^2 (\mathbf{n}_1 \cdot \mathbf{n}_2)^2} \right]^{-1/2} \quad (4)$$

$$\eta = \sqrt{\frac{(a^2 + c^2)^2}{4a^2c^2 + (a^2 - c^2)^2 |\mathbf{n}_1 \times \mathbf{n}_2|^2}} = [1 - \omega_1^2 (\mathbf{n}_1 \cdot \mathbf{n}_2)^2]^{-1/2} \quad (5)$$

$$\chi = \epsilon_a \left[ 1 + \frac{\omega_2 [(\hat{\mathbf{r}} \cdot \mathbf{n}_1)^2 + (\hat{\mathbf{r}} \cdot \mathbf{n}_2)^2] + 2\omega_2^2 (\mathbf{n}_1 \cdot \mathbf{n}_2)(\hat{\mathbf{r}} \cdot \mathbf{n}_1)(\hat{\mathbf{r}} \cdot \mathbf{n}_2)}{1 - \omega_2^2 (\mathbf{n}_1 \cdot \mathbf{n}_2)^2} \right]^2 \quad (6)$$

where  $\hat{\mathbf{r}} = \mathbf{r} / \|\mathbf{r}\|$  is the unit vector of the relative radial vector between their centers of mass, parameters  $\omega_1$  and  $\omega_2$  are functions of the given parameters:

$$\omega_1 = \frac{a^2 - c^2}{a^2 + c^2}, \quad \omega_2 = \frac{\sqrt{\epsilon_c} - \sqrt{\epsilon_a}}{\sqrt{\epsilon_c} + \sqrt{\epsilon_a}} \quad (7)$$

In the mesoscale simulations (Zhu et al., 2025), we use the force field fitted for the PMF data for open systems. Since face-to-face interaction is expected to dominate the aggregation behavior of the mesoscale particle assemblies, stronger interaction potential from the open system simulations is chosen to better manifest the physics. Ion and water exclusion was found in open systems, due to the connectedness of the interlayer and free space, which is closer to the mesoscale particles.

Hydrostatic compression was carried out for 10 dilute assemblies of 1000 particles randomly oriented in the initial configurations, from 0 to 1, 5, 25, and 125 atm. Unloading and reloading were also carried following the sequence of 25, 5, 1, 5, 25, and 125 atm. A typical equilibrated configuration after the compression is shown in Fig. 3. The particles are observed to form well-aligned stacks. The geometric structures of the particle assemblies were analyzed in terms of various parameters covered in the following sections. The typical results are also discussed together with their definitions.

For hydrostatically equilibrated systems, we also carried out strain-controlled 1D compression and shear simulations in the form of small strain increments applied as affine transformation of the simulated systems. The systems were then subjected to isothermal simulations to relax the stress. The stress increment after the relaxation is recorded as a response of the system to the applied strain increment. Through this process the stress–strain response of the systems were obtained, as exemplified by the typical result shown in Fig. 4. The initial 3 points of each stress–strain curves were previously used (Zhu, 2023; Zhu et al., 2025) to infer the small-strain stiffness of the systems. The reason for choosing the initial 3 points was that the particle stacking was found unchanged before and after the application of strains at this level. We assume the process is reversible since the mesostructure is not changed. From these prior works, we observe features in great resemblance to real clay behaviors:

- The assemblies start to exhibit inelastic deformation and hysteretic behavior at a low strain level of less than 0.1%.
- Elastic stiffness of the assemblies obtained from the stress–strain curves show trends similar to experimental data in terms of its dependence upon the confining pressure (Fig. 11-b).
- The elastic stiffness tensors of the assemblies exhibit orthotropic symmetry (Zhu et al., 2025; Zhu, 2023).

More details of the discussions related to the mesoscale simulations in comparison to real clay behaviors can be found in the prior works of the authors (Zhu et al., 2025; Zhu, 2023). In the current paper, the model results are primarily compared with the simulation data. The data are presented together with the development and discussions of the constitutive model in later sections.

## 2.2. Model parameters

### 2.2.1. Intrinsic interaction parameters

In the mesoscale simulations the particles are represented as axisymmetric rigid ellipsoids interacting through the Gay–Berne potential. The parameters involved in the derivation of the model include the lengths of the semiaxes,  $a$  and  $c$ ; the relative potential

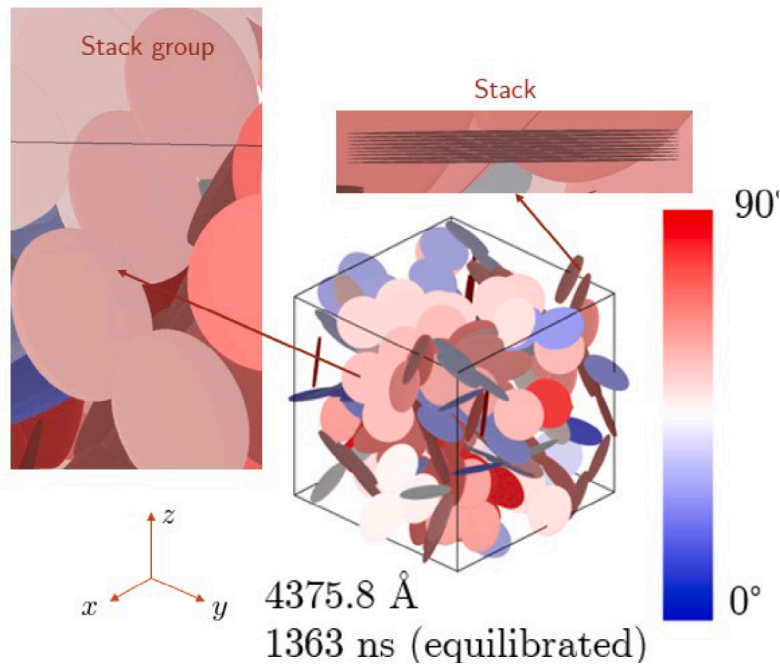


Fig. 3. Typical configuration of one of the systems equilibrated at 1 atm and 300 K. The color of the particles represents the angle between the normal vector of the particle and the  $z$  direction.

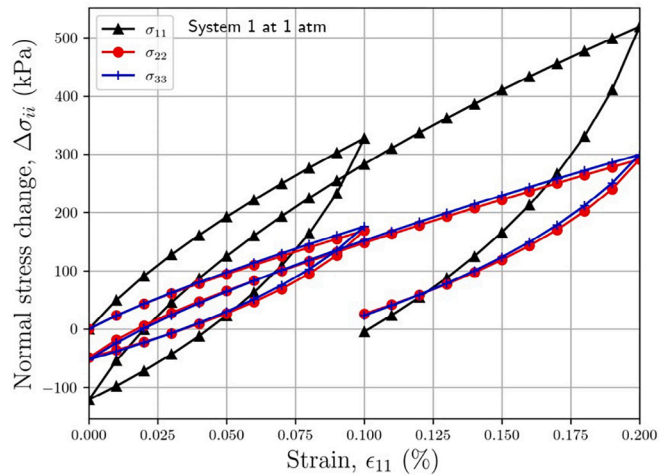


Fig. 4. Quasi-static stress-strain response for system 1 equilibrated at 1 atm subjected to strain increments in the 11 direction (Zhu et al., 2025).

well depth in the principal directions  $\epsilon_a$  and  $\epsilon_c$ ; and the van der Waals radius  $\sigma$  in the distance related term ( $u_L$ ). Since these parameters are intrinsic to the interparticle interactions and were obtained through nanoscale simulations (Zhu et al., 2022), they are treated as constants in the development of the model. The values are as summarized in the legend of Fig. 2.

### 2.2.2. Intra-stack parameters

A typical equilibrated configuration of the mesoscale systems is shown in Fig. 3. The plate-like particles are observed to form well-aligned groups along their central axis, which are referred to as *stacks*. Stacks then form end-to-end secondary structures, subsequently termed *stack groups*. Each assembly consists of relatively randomly oriented stack groups.

We develop a quantitative analyses of the equilibrated particle assembly by defining a stack in terms of the center-of-mass distance and angles between the unit normals of the adjacent particles, following Ebrahimi et al. (2014). Any pair of particles defined by radial vectors and unit normals  $(\mathbf{r}_1, \mathbf{n}_1)$  and  $(\mathbf{r}_2, \mathbf{n}_2)$  that belong to a same stack either satisfy:

**Table 1**

Parameters describing the mesostructures and constants for the pair potential appearing in the theoretical model.

Symbol	Significance	$\sim U_i$
<b>Intra-stack</b>		
$h$	Perpendicular alignment of particles inside a stack averaged over all intra-stack pairs of all stacks.	$U_1, U_{23}$
$\delta$	In-plane alignment of particles inside a stack averaged over all intra-stack pairs of all stacks	$U_1$
<b>Inter-stack</b>		
$\gamma_k, \mu_k, \sigma_k$	Parameters of the components of interstack pair correlation function $g(r)$ , $k = 1, 2, 3, 4$	$U_{2k}$
<b>Global</b>		
$\rho_{\text{stack}}$	Number density of stacks	All
$\bar{m}$	Average stack size	All
$\mathbb{F}$	Fabric tensor describing the preferred orientation of all particles in the system	$U_{24}$
<b>Intrinsic</b>		
$a, c$	In-plane radius and half thickness of the mesoscale ellipsoidal particles	All
$\epsilon_a, \epsilon_c$	Relative potential well depth in the edge-to-edge and face-to-face configurations	All
$\sigma$	Van der Waals radius and shift in the LJ term of GB potential	All

Notes: the constants here correspond to the PMF of illite open systems (Zhu et al., 2022, 2025), with which the mesoscale was carried out. The values are  $a = 503.0 \text{ \AA}$ ,  $c = 4.9 \text{ \AA}$ ,  $\epsilon_a = 37.0$ ,  $\epsilon_c = 2357.0$ ,  $\sigma = 9.8 \text{ \AA}$ . The coefficient  $\epsilon$  in the GB potential is set to 1 kcal/mol for convenience. The third column indicates the parts of potential energy of which the formulation uses a certain parameter.

### 1. Distance criterion:

$$|\mathbf{r}_1 - \mathbf{r}_2| \leq 13.75 \text{ \AA}$$

### 2. Angle criterion:

$$|\mathbf{n}_1 \cdot \mathbf{n}_2| \geq 0.95$$

or through transitivity, i.e.

- If particles  $i$  and  $j$  belong to the same stack, and particles  $j$  and  $k$  belong to the same stack, then particles  $i$  and  $k$  belong to the same stack.

The geometries of the particles within stacks are relatively well defined, so that in capturing the structures of the equilibrated mesoscale systems, we divide the structural properties into global, intra- and inter-stack properties, as defined in the following subsections and summarized in Table 1.

For each stack, the face-to-face distance and overlapping area are the two major factors affecting the potential energy between particle pairs within stacks. Since the particles are very well aligned within each stack (as shown in Fig. 3), we define perpendicular and in-plane alignment parameters  $h$  and  $\delta$ . They are defined with respect to a reference direction described by the average of the projection tensors of unit normals of the particles in a stack, i.e.  $\mathbf{N} = (\sum_{i \in \omega} \mathbf{n}_i \otimes \mathbf{n}_i) / m(\omega)$ , where  $\omega$  is the set of particles in a certain stack and  $m(\omega)$  is the size of the stack. The quantities  $h$  and  $\delta$  are defined as the average projection of relative radial vectors in the stacks with respect to  $\mathbf{N}$ :

$$h = \frac{1}{m(\omega) - 1} \sum_{i, j \in \omega} |\mathbf{N} \Delta \mathbf{r}_{ij}|, \quad \delta = \frac{1}{m(\omega)} \sum_{i \in \omega} |(\mathbf{1} - \mathbf{N}) \mathbf{r}'_i| \quad (8)$$

$h$  and  $\delta$  were stable for stacks of different sizes.

The tensor  $\mathbf{N}$  is not a projection tensor anymore. Strictly speaking, we need to find the principal direction  $\mathbf{n}^*$  of the deviatoric part of  $\mathbf{N}$  and redefine the projection tensor as  $\mathbf{n}^* \otimes \mathbf{n}^*$ , but since the particles are relatively well aligned as shown in Fig. 3, and as will be shown quantitatively in Fig. 5. The tensors,  $\mathbf{N}$  and  $\mathbf{n}^* \otimes \mathbf{n}^*$ , are approximately the same.

Fig. 5 shows the analysis for a typical configuration equilibrated at 5 atm. The level of  $\delta$  is much lower than  $h$  and the dimensions of the particles, which means that the particles within a stack are very well aligned along their axis of symmetry. Based on this observation, we assume  $h$  and  $\delta$  are constants for each equilibrated configuration.

### 2.2.3. Inter-stack parameters

In Fig. 3, the stacks are observed to form higher-order structures, which we call *stack groups*, where adjacent stacks are interlocked in an edge-to-edge position. The entire assembly can be viewed as a collection of stack groups. Due to presence of these structures, the stack pairs can be classified into categories. This is quantitatively reflected in the decomposition of inter-stack pair correlation functions  $g(r)$ , that are defined by a distribution function of the center-of-mass distance of stack pairs with respect to the volume element of  $r^2 dr$ , such that:

$$4\pi \rho_{\text{stack}} g(r) r^2 dr = dN_{\text{stack}} \quad (9)$$

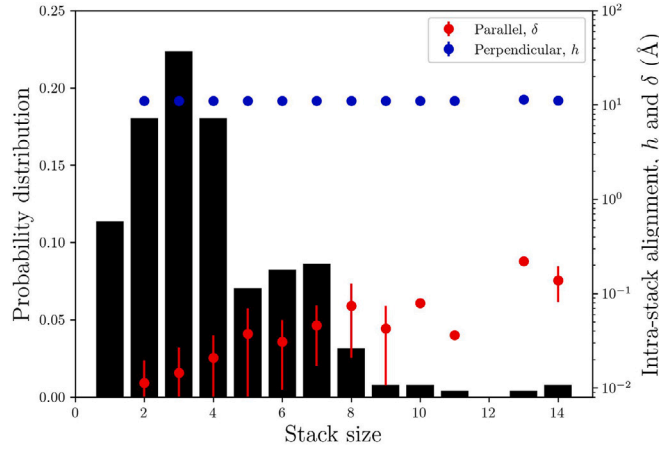


Fig. 5. Stack size distribution and the alignment variables (perpendicular  $h$  and parallel  $\delta$ ) for the equilibrated configuration of system 10 at 5 atm.

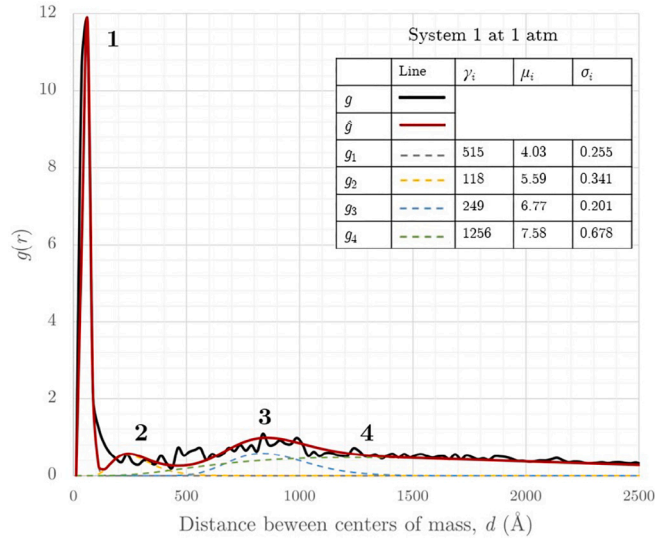


Fig. 6. Inter-stack pair correlation function for the one of the equilibrated configurations at 1 atm and the fitted curve with four components of lognormal distribution. Black curve is the result from simulation; red curve is the fit; and the colored curves are the four components.

where  $dN_{\text{stack}}$  is the number of stacks in the region between  $r$  and  $r + dr$ , and  $\rho_{\text{stack}}$  is the number density of stacks of the entire system, i.e.  $\rho_{\text{stack}} = N_{\text{stack}}/V$

Fig. 6 shows the inter-stack pair correlation function (pcf) for the equilibrated configuration. We use four weighted lognormal components to fit these results:

$$g(r) = \sum_{k=1}^p g_k(r) = \sum_{k=1}^p \frac{\gamma_k}{r \sigma_k \sqrt{2\pi}} \exp \left[ -\frac{(\ln r - \mu_k)^2}{2\sigma_k^2} \right] \tag{10}$$

where  $\gamma_k$  are the weight and  $\{\sigma_k, \mu_k\}$  the lognormal parameters of the components.

The decomposition reflects four types of stack pairs, observed in Fig. 3. They are shown schematically in Fig. 7 for clarity. Type 1 corresponds to two parallel stacks that are interlocked to the same third stack so that they are separated by more than one  $h$  and therefore not counted as a single stack. The characteristic center-of-mass distance is  $\bar{r}_1 = 20\sim 30 \text{ \AA}$ . Type 2 correspond to stack pairs at the brims of two stack groups. The two stacks are closer at one end and at a small angle with respect to each other. The characteristic length is  $\bar{r}_2 = 100\sim 200 \text{ \AA}$ . Type 3 are stacks that are interlocked end-to-end in a stack group, so that  $\bar{r}_3 = 800\sim 900 \text{ \AA}$ . Type 4 include the rest of the stack pairs, that are farther apart, with a characteristic distance  $\bar{r}_4 > 2a \sim 1000 \text{ \AA}$ . The relative orientation between the stack pairs of type 4 is represented by the fabric tensor, as derived analytically in Section 3.1. The final choice of four components is based on observational approach of detailed examination of all equilibrated configurations. The parameter set  $\{\gamma_k, \mu_k, \sigma_k\}_{k=1}^4$  is the major descriptor of the inter-stack properties of the assemblies.

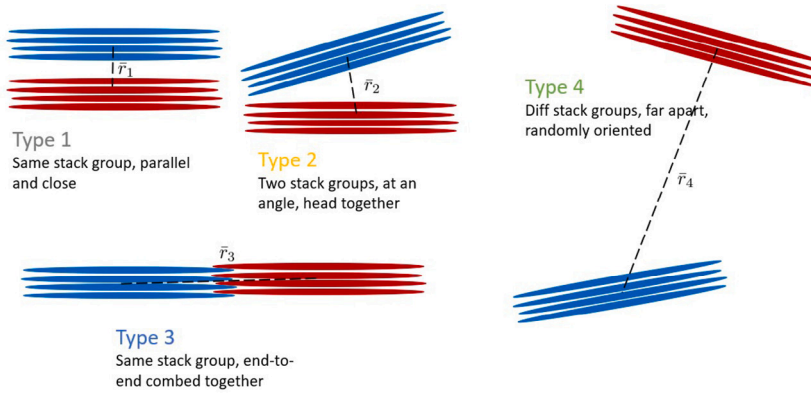


Fig. 7. Schematic representation of four types of stack pairs corresponding to lognormal components of the pair correlation function. Different colors represent types of neighbors corresponding to different characteristic lengths between centers of mass, as shown in Fig. 6.

#### 2.2.4. Global parameters

Apart from the inter- and intra-stack properties, there are a few other properties that describe the assembly as a whole. The packing density of the system is jointly described by the number density of the stacks  $\rho_{\text{stack}}$  and the average stack size  $\bar{m}$ . The overall orientation of the particles is described with fabric tensor, defined as, the average of the projection tensors of the unit normals of all particles:

$$\mathbb{F} = \langle \mathbf{n} \otimes \mathbf{n} \rangle = \frac{1}{N_{\text{particle}}} \sum_{i=1}^{N_{\text{particle}}} \mathbf{n}_i \otimes \mathbf{n}_i \quad (11)$$

which is conveniently a real symmetric tensor that allows spectral decomposition:

$$\mathbb{F} = \sum_{i=1}^3 \lambda_i \mathbf{u}_i \otimes \mathbf{u}_i \quad (12)$$

It also has a unit trace so that:

$$\text{tr } \mathbb{F} = \lambda_1 + \lambda_2 + \lambda_3 = 1 \quad (13)$$

### 3. Model formulation

The information contained in the parameter set

$$\Lambda = \{h, \delta, \{\gamma_k, \mu_k, \sigma_k\}_{k=1}^4, \rho_{\text{stack}}, \bar{m}, \mathbb{F}\} \quad (14)$$

presented in the previous subsections characterizes the mesoscale structure of an equilibrated particle assembly. To develop a constitutive elastic model of the assemblies, it is crucial to find the functional relation between the potential energy of the system, the parameter set  $\Lambda$  and small/recoverable strain (in terms of deformation gradient  $\mathbf{F}$ ), i.e.  $U(\Lambda, \mathbf{F})$ . The elastic stiffness tensor can then be calculated as a second order derivative of the specific potential energy to the infinitesimal strain tensor  $\mathbf{E} = (\mathbf{F} + \mathbf{F}^T)/2$ :

$$\mathbb{C} = \frac{1}{V} \frac{\partial^2 U}{\partial \mathbf{E} \partial \mathbf{E}} \quad (15)$$

Therefore, the formulation is divided into the following two parts:

1. Homogenization: ‘static’ relation between the potential energy of a system and the parameter set, i.e.  $U(\Lambda)$
2. Perturbation: relation describing the elastic change of the parameter set  $\Lambda$  under a small affine transformation defined by deformation gradient  $\mathbf{F}$ , i.e.  $\Lambda_p(\Lambda, \mathbf{F})$

The two parts of the formulation give rise to the final form of  $U(\Lambda, \mathbf{F})$ .

#### 3.1. Homogenization scheme

In the following formulation, the potential energy of the system is divided into intra- and inter-stack parts based on the discussion in previous sections, i.e.,

$$U = U_1 + U_2 \quad (16)$$

$$U_2 = U_{21} + U_{22} + U_{23} + U_{24} \quad (17)$$

### 3.1.1. Intra-stack potential energy, $U_1$

Stacks of particles are highly aligned unit inside an assembly. The intra-stack potential energy is therefore mainly due to the face-to-face potential energy within adjacent pairs of particles in a stack. The parallel alignment  $\delta$  was found to be small compared with the in-plane dimension of the particles ( $\delta/a \ll 1 : 500$ ). An averaged level of face-to-face overlapping area among them can be approximated through:

$$A(\delta) = 2a^2 \arccos \frac{\delta}{2a} - \delta \sqrt{a^2 - (\delta/2)^2} \quad (18)$$

$$= 2a^2 \left( \frac{\pi}{2} - \frac{\delta}{2a} \right) - \delta a + o \left[ \left( \frac{\delta}{a} \right)^3 \right] \approx \pi a^2 - 2\delta a \quad (19)$$

For a stack with  $m$  particles, there are  $m-l$  pairs of particles that are separated by  $l-1$  particles. However, many of the associated terms therewith are negligible. We have found that the distance between the direct neighbors correspond to the minimum of the term  $u_{\text{LJ}}$ , so that  $r_m = 2c + (\sqrt[6]{2} - 1)\sigma$ . For pairs separated by  $l-1 = 0, 1, 2, 3, 4 \dots$  particles, we have:

$$u_{\text{LJ}}^{\text{ff}}(r_m) = 4\epsilon \left[ \left( \frac{\sigma}{r_m} \right)^{12} - \left( \frac{\sigma}{r_m} \right)^6 \right] = -\epsilon \quad (20)$$

$$u_{\text{LJ}}^{\text{ff}}(2r_m) = 4\epsilon \left[ \left( \frac{\sigma}{2r_m} \right)^{12} - \left( \frac{\sigma}{2r_m} \right)^6 \right] = -\frac{2^7 - 1}{2^{12}} \epsilon \approx -\frac{\epsilon}{32.25} \quad (21)$$

$$u_{\text{LJ}}^{\text{ff}}(3r_m) = 4\epsilon \left[ \left( \frac{\sigma}{3r_m} \right)^{12} - \left( \frac{\sigma}{3r_m} \right)^6 \right] = -\frac{2 \times 3^6 - 1}{3^{12}} \epsilon \approx -\frac{\epsilon}{364.8} \quad (22)$$

$$u_{\text{LJ}}^{\text{ff}}(4r_m) = 4\epsilon \left[ \left( \frac{\sigma}{4r_m} \right)^{12} - \left( \frac{\sigma}{4r_m} \right)^6 \right] = -\frac{2^{13} - 1}{2^{24}} \epsilon \approx -\frac{\epsilon}{2048} \quad (23)$$

where  $\sigma = 9.8 \text{ \AA}$ ,  $\epsilon = 1 \text{ kcal/mol}$  are the intrinsic parameters related to the distance related term in the GB potential.

Eqs. (20)–(23) indicate that the face-to-face potential energy associated with pairs separated by 3 particles is more than 3 orders of magnitude smaller than the contribution of the directly adjacent pairs. In this model, we only consider up to pairs separated by two particles. Besides, as a first approximation, all stacks are considered to have the average stack size  $\bar{m}$ . The intra-stack potential energy for the entire system would be:

$$U_1 = N_{\text{stack}} [(\bar{m}-1)u_{\text{LJ}}^{\text{ff}}(h) + (\bar{m}-2)u_{\text{LJ}}^{\text{ff}}(2h) + (\bar{m}-3)u_{\text{LJ}}^{\text{ff}}(3h)] \eta \chi A(\delta) / (\pi a^2) \quad (24)$$

$$\approx 4\epsilon \epsilon_c \rho_{\text{stack}} V \frac{a^2 + c^2}{2ac} (1.034\bar{m} - 1.070) \left[ \left( \frac{\sigma}{h} \right)^{12} - \left( \frac{\sigma}{h} \right)^6 \right] \left( 1 - \frac{2\delta}{\pi a} \right) \quad (25)$$

where  $a = 503 \text{ \AA}$ ,  $c = 4.9 \text{ \AA}$  are the GB parameters describing the semiaxes of the particles,  $\bar{m}$  is the average stack size,  $h$  and  $\delta$  are the intrastack alignment.  $\eta$  and  $\chi$  are the orientation and shape dependent terms in the GB potential.

### 3.1.2. Inter-stack potential energy

The inter-stack potential energy is controlled by the relative positions between the stacks, which is approximately described by the inter-stack pair correlation function  $g(r)$ . It is also related to the preferred orientations, as described by the fabric tensor  $\mathbb{F} = \langle \mathbf{n} \otimes \mathbf{n} \rangle$ . Based on the discussions in the previous sections, we divide the inter-stack energy further into four parts, according to the type of stack pairs in consideration (as shown in Fig. 7), as given in Eq. (16).

Each part of the potential energy can be calculated in the following general form:

$$U_{2i} = 2\pi \rho_{\text{stack}}^2 V N_{\text{pair}} \int_0^\infty U_{\text{GB}}(\mathbf{r}, \mathbf{n}_1, \mathbf{n}_2) g_i(r) r^2 dr, \quad i = 1, 2, 3, 4 \quad (26)$$

where  $N_{\text{pair}}$  is the averaged number of pairs of particles involved in the inter-stack interaction between each pair of stacks. Since the geometric relation for each type of stack pair is known, the integration can be further specialized according to the different representative inter-stack configurations for each part. In fact the three multiplicative parts of the Gay–Berne potential  $u_{\text{LJ}}$ ,  $\eta$ , and  $\chi$  (as described in the Appendix A), which are dependent upon  $\mathbf{r}, \mathbf{n}_1, \mathbf{n}_2$  for the interacting particle pairs, can be reduced to a function of  $r = \|\mathbf{r}\|$  alone, so that the integration can be analytically evaluated. For a typical interacting pairs for two stacks in consideration, the LJ term of the Gay–Berne potential is always close to its minimum ( $-\epsilon = -1 \text{ kcal/mol}$ ) in equilibrated configurations for the  $U_{21}$ ,  $U_{22}$ , and  $U_{23}$ , so that in the corresponding derivations, we assume  $u_{\text{LJ}} = -\epsilon$ .

**3.1.2.1.  $U_{21}$  and  $U_{22}$ .** The relative configuration of this pair of particles is as shown in Fig. 7. The term  $U_{\text{GB}}(\mathbf{r}, \mathbf{n}_1, \mathbf{n}_2)$  can then be written as a function of  $r$  alone, thus enable analytical form for the integration. The formulation is a result of the following assumptions:

1. The effective range of  $r$  for  $U_{21}$  and  $U_{22}$  is less than the in-plane radius  $a$  of the particles, so that the terms  $\eta$  and  $\chi$  can be approximated by simple rational functions.
2.  $N_{\text{pair}} = \bar{m}^2$  pairs of particles contribute to this part of the potential energy.
3. The LJ term of the GB potential is close to  $-1$  in equilibrium for  $U_{21}$  and  $U_{22}$ .

The relative configuration of a representative pair of particles (as shown in Fig. 8) can be solely determined by the center-of-mass distance  $r$  between the interacting particles, which is approximately equal to the center-of-mass distance between the interacting stacks:

$$\hat{\mathbf{r}} \cdot \mathbf{n}_1 = \hat{\mathbf{r}} \cdot \mathbf{n}_2 = \cos \frac{\alpha}{2} = \sqrt{1 - \frac{r^2}{4a^2}}, \quad \mathbf{n}_1 \cdot \mathbf{n}_2 = \cos \alpha = 1 - \frac{r^2}{2a^2} \quad (27)$$

Putting this result into Eq. (3), the GB parameters  $\eta$  and  $\chi$  can be given as functions of  $r$  alone (for  $r < 2a$ ):

$$\eta = \left[ 1 - \omega_1^2 \left( 1 - \frac{r^2}{2a^2} \right)^2 \right]^{-1/2} \quad (28)$$

$$\chi = \epsilon_c \left[ 1 + \frac{\omega_2}{1 - \omega_2} \frac{r^2}{2a^2} \right]^{-2} \quad (29)$$

We have  $\eta(r = 0) = (a^2 + c^2)/2ac$  and  $\eta(r = 2a) = 1$ . Similarly,  $\chi(r = 0) = \epsilon_c$  and  $\chi(r = 2a) = \epsilon_a$ . For  $r \gtrsim 2a$ , the stack pairs can no longer be considered belonging to this configuration. To further simplify the functions for evaluation of the integration, we can use simple rational functions as an approximation. In this case:

$$\hat{\eta} = \eta_1 + \frac{\eta_2}{r^2 + v_\eta}, \quad \hat{\chi} = \chi_1 + \frac{\chi_2}{r^2 + v_\chi} \quad (30)$$

If we evaluate the key values at  $r = 0, a, 2a$  for  $\eta, \chi$  and  $r = 0, a, \infty$  for  $\hat{\eta}, \hat{\chi}$ , we have:

$r$	$\eta$	$\hat{\eta}$
0	$\eta_{\max} = (a^2 + c^2)/2ac$	$\eta_1 + \eta_2/v_\eta$
$a$	$\eta_{\text{mid}} = (1 - \omega_1^2/4)^{-1/2}$	$\eta_1 + \eta_2/(a^2 + v_\eta)$
$2a$	$\eta_{\min} = 1$	$\eta_1$
$\infty$		$\eta_1$
$r$	$\chi$	$\hat{\chi}$
0	$\chi_{\max} = \epsilon_c$	$\chi_1 + \chi_2/v_\chi$
$a$	$\chi_{\text{mid}} = \epsilon_c \left[ 1 + \omega_2/(2(1 - \omega_2)) \right]^{-2}$	$\chi_1 + \chi_2/(a^2 + v_\chi)$
$2a$	$\chi_{\min} = \epsilon_a$	$\chi_1$
$\infty$		$\chi_1$

If we equate the quantities in each row, we can solve out the values for the parameters in the approximate functions:

$\eta_1 = \eta_{\min}$	$\eta_2 = v_\eta(\eta_{\max} - \eta_{\min})$	$v_\eta = \frac{\eta_{\text{mid}} - \eta_{\min}}{\eta_{\max} - \eta_{\text{mid}}} a^2$
$\chi_1 = \chi_{\min}$	$\chi_2 = v_\chi(\chi_{\max} - \chi_{\min})$	$v_\chi = \frac{\chi_{\text{mid}} - \chi_{\min}}{\chi_{\max} - \chi_{\text{mid}}} a^2$

The integration in Eq. (26) can be transformed into (for  $i = 1$  or  $2$ ):

$$\int_0^\infty U_{\text{GB}}(\mathbf{r}, \mathbf{n}_1, \mathbf{n}_2) g_i(r) r^2 dr = \int_0^\infty u_{\text{LJ}} \eta \chi g_i(r) r^2 dr \approx - \int_0^\infty \epsilon \hat{\eta} \hat{\chi} g_i(r) r^2 dr \quad (33)$$

$$= - \int_0^\infty \epsilon \left( \eta_1 \chi_1 + \frac{c_\eta}{r^2 + v_\eta} + \frac{c_\chi}{r^2 + v_\chi} \right) g_i(r) r^2 dr \quad (34)$$

where

$$c_\eta = \chi_1 \eta_2 + \frac{\chi_2 \eta_2}{v_\chi - v_\eta} \quad (35)$$

$$c_\chi = \eta_1 \chi_2 + \frac{\chi_2 \eta_2}{v_\eta - v_\chi} \quad (36)$$

The integration above contain integrations in the form of:

$$I_1 = \int_0^\infty \frac{1}{\sigma \sqrt{2\pi r}} \frac{r^2}{r^2 + v} \exp \left( -\frac{(\ln r - \mu)^2}{2\sigma^2} \right) dr \quad (37)$$

corresponding to the first type of integral in Appendix B, which can be approximately evaluated as Eq. (B.16). With this relation, the final form of these two parts of the potential energy is given by ( $i = 1, 2$ ):

$$U_{2i} = -2\pi\epsilon\rho_{\text{stack}}^2 V \bar{m}^2 \gamma_i \left[ \eta_1 \chi_1 \exp(2\mu_i + 2\sigma_i^2) + c_\eta L \left( \frac{2\mu_i - \ln v_\eta}{\sqrt{1 + \pi\sigma_i^2/2}} \right) + c_\chi L \left( \frac{2\mu_i - \ln v_\chi}{\sqrt{1 + \pi\sigma_i^2/2}} \right) \right] \quad (38)$$

where  $L(x) = 1/(1 + \exp(-x))$  is the logistic function and all the other coefficients are given above.

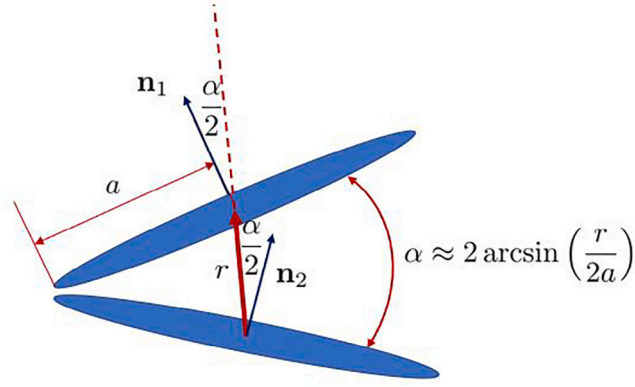


Fig. 8. Schematic representation of a representative pair of particles involved in inter-stack interaction components  $U_{21}$  and  $U_{22}$ .

3.1.2.2.  $U_{23}$ . The third group comprise pairs of stacks that are approximately parallel and inter-laced, as shown in Figs. 7 and 9. Based on these observations, the derivation for this part is based on the following assumptions:

1. Representative particle pair is parallel with perpendicular alignment of  $h/2$  and parallel alignment of  $\bar{r}_3 = \langle r \rangle_{g_3} = \exp(\mu_3 + 5\sigma_3^2/2)$
2. A stack contains  $\bar{m}$  particles, yielding  $N_{\text{pair}} = 2\bar{m} - 1$  of representative pairs

Consequently, the dot products in Eq. (3) are:

$$\mathbf{n}_1 \cdot \mathbf{n}_2 = 1, \quad |\hat{\mathbf{r}} \cdot \mathbf{n}_1| = |\hat{\mathbf{r}}_2 \cdot \mathbf{n}_2| \approx \frac{h}{2\bar{r}_3} \quad (39)$$

so that:

$$\eta = \frac{a^2 + c^2}{2ac} \quad (40)$$

$$\chi = \left( 1 + \frac{\sqrt{\epsilon_c} - \sqrt{\epsilon_a}}{2\sqrt{\epsilon_a}} \frac{h^2}{2\bar{r}_3^2} \right)^2 \quad (41)$$

$$u_{\text{LJ}}(\bar{r}_3, h/2) = 4\epsilon \left[ \left( \frac{\sigma}{\bar{r}_3 - \bar{\sigma}(\bar{r}_3, h/2) + \sigma} \right)^{12} - \left( \frac{\sigma}{\bar{r}_3 - \bar{\sigma}(\bar{r}_3, h/2) + \sigma} \right)^6 \right] \quad (42)$$

$$\bar{\sigma}(\bar{r}_3, h/2) = 2a \left[ 1 + \frac{\omega_1}{1 - \omega_1} \frac{h^2}{2\bar{r}_3^2} \right]^{-1/2} \quad (43)$$

The resulting formulation is then given by:

$$\begin{aligned} U_{23} &= 2\pi\rho_{\text{stack}}^2 V(2\bar{m} - 1)u_{\text{LJ}}(\bar{r}_3, h/2) \int \eta\chi g_3(r)r^2 dr \\ &= 2\pi\rho_{\text{stack}}^2 V\gamma_3\epsilon_a(2\bar{m} - 1)\exp(2\mu_3 + 2\sigma_3^2) \frac{a^2 + c^2}{2ac} \\ &\quad \left( 1 + \frac{\sqrt{\epsilon_c} - \sqrt{\epsilon_a}}{2\sqrt{\epsilon_a}} \frac{h^2}{2\bar{r}_3^2} \right)^2 u_{\text{LJ}}(\bar{r}_3, h/2) \end{aligned} \quad (44)$$

3.1.2.3.  $U_{24}$ . The fourth part describes stack pairs that are far from each other and randomly oriented with respect to each other. The GB term in the integration cannot be simply reduced to univariate functions as in the cases of  $U_{21}$ ,  $U_{22}$ , and  $U_{23}$ . However, the average orientation of particles at each point is described by the fabric tensor, so that the preferred orientation can be treated as a superposed state of three proportions of particles pointing at directions defined by the eigenvectors of the tensor. Referring to the discussion on the fabric tensor above, its property of symmetry and unit trace allows a spectral decomposition  $\mathbb{F} = \sum \lambda_i \mathbf{u}_i \otimes \mathbf{u}_i$ , where  $\{\mathbf{u}_i\}_{i=1}^3$  forms an orthonormal basis and  $\sum \lambda_i = 1$ . With this notion, the derivation can be based on the following assumptions:

1. Each stack contains  $\bar{m}$  particles, and therefore  $N_{\text{pair}} = \bar{m}^2$
2. Each material point in space carries a superposed state of three portions of particles. The directions are defined by the eigenvectors  $\{\mathbf{u}_i\}_{i=1}^3$  of the fabric tensor, with corresponding proportions defined by the eigenvalues  $\lambda_i$ .
3. The characteristic length  $\bar{r}_4$  is greater than the dimension of the particles.

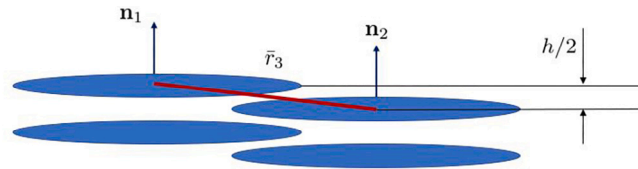


Fig. 9. Schematic representation of the configuration of particle pairs involved in inter-stack interaction component  $U_{23}$ .

Assumption 2 indicates that the GB potential term in the integration contains a summation of 9 terms:

$$\sum_{i,j} \lambda_i \lambda_j U_{GB}(\mathbf{u}_i, \mathbf{u}_j, \mathbf{r}) \quad (45)$$

Assumption 3 allows an approximation of the LJ term of the GB potential:

$$u_{LJ} \approx 4\epsilon \left[ \left( \frac{\sigma}{r} \right)^{12} - \left( \frac{\sigma}{r} \right)^6 \right] \quad (46)$$

Other multiplicative components related to the shape and orientation of the particles can be simplified by the orthonormality of  $\{\mathbf{u}_i\}_{i=1}^3$ . For a pair of particles with radial vector  $\mathbf{r} (= r\hat{\mathbf{r}})$  and unit normals  $\mathbf{u}_i$  and  $\mathbf{u}_j$

$$\eta = \sqrt{\frac{(a^2 + c^2)^2}{4a^2c^2 + (a^2 - c^2)^2(1 - \delta_{ij})}} = \sqrt{\frac{(a^2 + c^2)^2}{(a^2 + c^2)^2 - (a^2 - c^2)^2\delta_{ij}}} = \sqrt{\frac{1}{1 - \omega_1^2\delta_{ij}}} \quad (47)$$

$$\chi = \epsilon_a \left[ 1 + \frac{\omega_2((\hat{\mathbf{r}} \cdot \mathbf{u}_i)^2 + (\hat{\mathbf{r}} \cdot \mathbf{u}_j)^2) + 2\omega_2^2\delta_{ij}(\hat{\mathbf{r}} \cdot \mathbf{u}_i)(\hat{\mathbf{r}} \cdot \mathbf{u}_j)}{1 - \omega_2^2\delta_{ij}} \right]^2 \quad (48)$$

where  $\omega_1 = (a^2 - c^2)/(a^2 + c^2)$  and  $\omega_2 = (\sqrt{\epsilon_c} - \sqrt{\epsilon_a})/(\sqrt{\epsilon_c} + \sqrt{\epsilon_a})$ .

The resulting formulation of this part of the potential energy is:

$$U_{24} = \pi\epsilon\epsilon_a\rho_{\text{stack}}^2 V \bar{m}^2 S^r (S^{\parallel} + S^{\perp}) \quad (49)$$

where the terms  $S^r$ ,  $S^{\parallel}$ , and  $S^{\perp}$  are given by:

$$S^r = 4\gamma_4[\sigma^{12}\exp(-10\mu_4 + 50\sigma_4^2) - \sigma^6\exp(-4\mu_4 + 8\sigma_4^2)] \quad (50)$$

$$S^{\parallel} = (\lambda_1^2 + \lambda_2^2 + \lambda_3^2) \frac{a^2 + c^2}{2ac} \left( 1 + \frac{2}{3}A + \frac{1}{5}A^2 \right) \quad (51)$$

$$S^{\perp} = (\lambda_1\lambda_2 + \lambda_2\lambda_3 + \lambda_3\lambda_1) \left( 1 + \frac{8}{3}B + \frac{16}{15}B^2 \right) \quad (52)$$

where  $A = 2\omega_2/(1 - \omega_2) = (\sqrt{\epsilon_c} - \sqrt{\epsilon_a})/\sqrt{\epsilon_a}$  and  $B = \omega_2 = (\sqrt{\epsilon_c} - \sqrt{\epsilon_a})/(\sqrt{\epsilon_c} + \sqrt{\epsilon_a})$ .

### 3.1.3. Evaluation

Fig. 10 compares the mean values of the intra-stack, inter-stack and total potential energies for hydrostatic compression of 10 particle assemblies (1) directly from the numerical simulations and (2) based on the proposed model. The theoretical model is in very good agreement with the intra-stack potential energy but overestimates the inter-stack potential energy (in terms of absolute value). However the magnitude of the interstack potential energy is small (roughly 1/10) compared to the intra-stack energy so that the relative error in total potential energy is within 10%.

Following this model, the calculated components of the potential energy averaged over the 10 systems at 1 atm are  $U_1 = -8.81 \times 10^7$ ,  $U_2 = -6.24 \times 10^6$ ,  $U_{21} = -1.66 \times 10^6$ ,  $U_{22} = -8.05 \times 10^4$ ,  $U_{23} = -4.50 \times 10^6$ , and  $U_{24} = 4.22 \times 10^{-3}$  kcal/mol. The division is similar at other confining pressures, highlighting that most of the potential energy associated with the stacks themselves (intra-stack PE). This is due to the difference in order of magnitude between the face-to-face and edge-to-edge interactions. The intra-stack potential energy is dominated by face-to-face interactions and the stack structures dominates the local geometry of the assemblies. The inter-stack potential energy is roughly one tenth of the intra-stack energy. Within the inter-stack energy, types 1 and 3 contribute the most. The contribution from type 2 is of lesser importance and from type 4 negligible.

As is shown in Fig. 10, potential energy shows near linear dependence with the logarithm of confining pressure. In the mesoscale simulation paper by the Authors (Zhu et al., 2025) a linear dependence between void ratio and logarithm of confining pressure was found, where  $\Delta e \sim -2.7224 \lg p$ . The two results indicate a linear dependence between the potential energy and the void ratio. Qualitatively, we obtain the following result:

$$U \sim 2.5 \times 10^6 e - 1.1 \times 10^8 \sim 3.1\rho^{-1} - 1.1 \times 10^8 \quad (53)$$

where  $\rho := N/V$  is the number density of the particles (unit:  $\text{\AA}^{-3}$ , and that  $N = 1000$ ), reflecting the packing density of the system, so that the potential energy density is related through:

$$u = \frac{U}{V} \sim \frac{3.1}{\rho V} - \frac{1.1 \times 10^8}{V} \sim -1.1 \times 10^5 \rho + 3.1 \times 10^{-3} \quad (54)$$

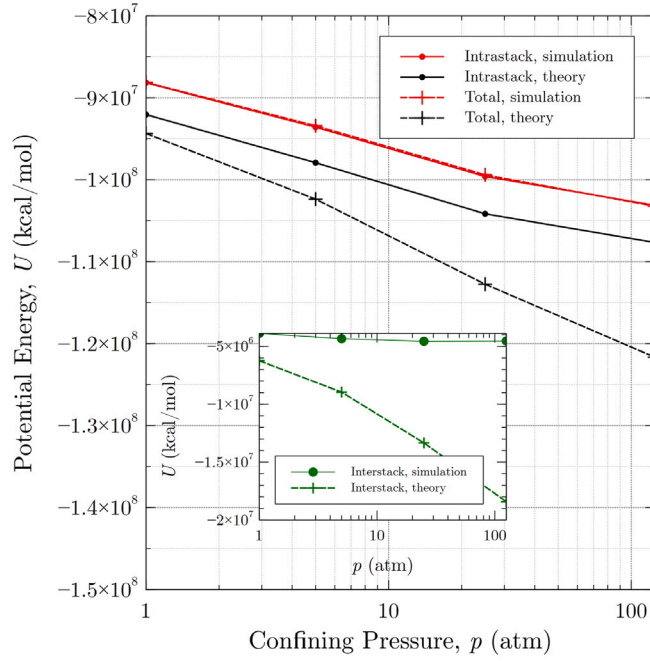


Fig. 10. Comparison of the evolution of potential energy between simulation results and theoretical predictions.

Notes: main plot shows the intrastack and total potential energy and the inset interstack. All data points represent results averaged over 10 systems.

That is to say that the energy density varies linearly with the packing density within the simulated range of confining pressures.

### 3.2. Perturbation scheme

We assume elastic deformation to be an infinitesimal affine transformation. In order to evaluate the change of potential energy due to such transformations, we need to recapitulate on some of the rules of transformation for material fibers and unit normals that can be found in continuum mechanics texts, e.g. Gurtin et al. (2010) and Liu (2002):

Affine transformation can be defined with respect to a fixed point  $\mathbf{O}$  in space as:

$$\mathbf{x} = \mathbf{F}(\mathbf{X} - \mathbf{O}) + \mathbf{O} \quad (55)$$

where  $\mathbf{F}$  is a constant tensor not dependent upon  $\mathbf{X}$ . For two material points  $\mathbf{X}$  and  $\mathbf{Y}$ , the deformed fiber is related to the undeformed through:

$$\mathbf{x} - \mathbf{y} = \mathbf{F}(\mathbf{X} - \mathbf{Y}) \quad (56)$$

Infinitesimally,  $d\mathbf{x} = \mathbf{F}d\mathbf{X}$ , i.e.  $\mathbf{F}$  is the deformation gradient common to all points in space.

For two undeformed infinitesimal fibers defining a surface,  $d\mathbf{X}$  and  $d\mathbf{Y}$ , the unit normal associated with them is:

$$\mathbf{n}_R = \frac{1}{a_R} d\mathbf{X} \times d\mathbf{Y} \quad (57)$$

where  $a_R = |d\mathbf{X} \times d\mathbf{Y}|$ .<sup>1</sup>

For the deformed area, the unit normal is:

$$\mathbf{n} = \frac{1}{a} d\mathbf{x} \times d\mathbf{y} = \frac{1}{a} \mathbf{F}d\mathbf{X} \times \mathbf{F}d\mathbf{Y} = \frac{1}{a} \mathbf{F}^{\text{cof}} d\mathbf{X} \times d\mathbf{Y} = \frac{a_R}{a} \mathbf{F}^{\text{cof}} \mathbf{n}_R \quad (58)$$

where  $\mathbf{F}^{\text{cof}} = \mathbf{J}\mathbf{F}^{-\text{T}}$  ( $\mathbf{J} = \det \mathbf{F}$  being the Jacobian of deformation gradient) is the *cofactor* of the deformation gradient  $\mathbf{F}$ . The transformed unit normal is then given by:

$$\mathbf{n} = \frac{\mathbf{F}^{-\text{T}} \mathbf{n}_R}{|\mathbf{F}^{-\text{T}} \mathbf{n}_R|} \quad (59)$$

In summary,  $\mathbf{F}$  maps the tangent vectors and  $\mathbf{F}^{-\text{T}}$  maps the normal vectors.

<sup>1</sup> Here,  $\times$  denotes the cross product, so that  $\mathbf{a} \times \mathbf{b} = \epsilon_{ijk} a_i b_j \mathbf{e}_k$ , where  $\epsilon_{ijk}$  is the Levi-Civita symbol.

With the help of relations given in Eqs. (56) and (59), we can deduce the change brought about to the parameter set by an affine transformation corresponding to the deformation gradient  $\mathbf{F}$ . The elastic constants can then be derived directly from Eq. (15).

The influence of deformation on the parameters depends on the particle orientation and the relative positions between particles. Here we compute the perturbed potential energy, by considering the proportion and orientation given by the spectral decomposition of the original fabric tensor (Eq. (11)). In the discussion in this section, the quantities and parameters in the unperturbed configuration are attached with a subscript of 'R'. For convenience, here we point out the convention for index  $l \in \{1, 2, 3\}$ , and indices  $(l, p, q) \in \{(1, 2, 3), (2, 3, 1), (3, 1, 2)\}$

### 3.2.1. Number density and stack size distribution

Since the average distance between stacks is much larger than the distance between particles within a stack, we assume an infinitesimal transformation does not change the grouping of particles, and therefore does not change the stack size distribution and the total number of stacks. However, the number density will be changed with the change in volume. This is characterized by:

$$dv = J dv_R \quad (60)$$

so that,

$$\rho_{\text{stack}}(\mathbf{F}) = \frac{\rho_{\text{stackR}}}{J} \quad (61)$$

where  $J = \det \mathbf{F}$ .

### 3.2.2. Stack alignment

Considering a pair of particles in any stack, the vector connecting the centers of mass of them is  $\mathbf{r}_R$ , and the averaged unit normal of the stack is  $\mathbf{n}_R$ . The original perpendicular stack alignment is  $h_R = |(\mathbf{n}_R \otimes \mathbf{n}_R)\mathbf{r}_R| = |\mathbf{n}_R \cdot \mathbf{r}_R|$  and in-plane alignment is  $\delta_R = |(\mathbf{1} - \mathbf{n}_R \otimes \mathbf{n}_R)\mathbf{r}_R|$ . Under the influence of an affine transformation  $\mathbf{F}$ , the vectors are transformed as  $\mathbf{r}(\mathbf{F}) = \mathbf{F}\mathbf{r}_R$  and  $\mathbf{n}(\mathbf{F}) = \mathbf{F}^{-T}\mathbf{n}_R/|\mathbf{F}^{-T}\mathbf{n}_R|$ . The perpendicular and in-plane stack alignments for the deformed system are:

$$h(\mathbf{F}) = \frac{|\mathbf{F}^{-T}\mathbf{n}_R \cdot \mathbf{F}\mathbf{r}_R|}{|\mathbf{F}^{-T}\mathbf{n}_R|} = \frac{|\mathbf{F}^T\mathbf{F}^{-T}\mathbf{n}_R \cdot \mathbf{r}_R|}{|\mathbf{F}^{-T}\mathbf{n}_R|} = \frac{h_R}{|\mathbf{F}^{-T}\mathbf{n}_R|} \quad (62)$$

$$\delta(\mathbf{F}) = \sqrt{r^2 - h^2} = \sqrt{(\mathbf{F}\mathbf{r}_R)^2 - \frac{h_R^2}{|\mathbf{F}^{-T}\mathbf{n}|^2}} \quad (63)$$

Considering the spectral decomposition of unperturbed fabric tensor  $\mathbb{F} = \sum \lambda_i \mathbf{u}_i \otimes \mathbf{u}_i$ , the intra-stack particle pairs having different orientations are affected differently by each perturbation. Considering a pair of particles with vertical distance  $h_R$ , parallel offset  $\delta_R$  and common unit normal  $\mathbf{u}_i$  ( $\in \{\mathbf{u}_i\}_{i=1}^3$ ), the relative position of the pair of particle is uniquely determined. If we further specify the orientation of the parallel component of the radial vector between the centers of mass of the particles,  $(\mathbf{1} - \mathbf{u}_i \otimes \mathbf{u}_i)\mathbf{r}_R$  through specifying the Eulerian angle of intrinsic rotation  $\psi \in [0, 2\pi)$ .

$$\mathbf{r}_R = h_R \mathbf{u}_i + \delta_R (\cos \psi \mathbf{u}_p + \sin \psi \mathbf{u}_q), \quad (64)$$

Then the average perturbed stack alignments for proportion in direction  $\mathbf{u}_i$  are:

$$h_i(\mathbf{F}) = \frac{h_R}{|\mathbf{F}^{-T}\mathbf{u}_i|} \quad (65)$$

$$\delta_i(\mathbf{F}) = \sqrt{\frac{1}{2\pi} \int_0^{2\pi} \left[ (\mathbf{F}\mathbf{r}_R)^2 - \frac{h_R^2}{|\mathbf{F}^{-T}\mathbf{u}_i|^2} \right] d\psi} \quad (66)$$

$$= \sqrt{h_R^2 \left( |\mathbf{F}\mathbf{u}_i|^2 - \frac{1}{|\mathbf{F}^{-T}\mathbf{u}_i|^2} \right) + \frac{\delta_R^2}{2} (|\mathbf{F}\mathbf{u}_p|^2 + |\mathbf{F}\mathbf{u}_q|^2)} \quad (67)$$

### 3.2.3. Inter-stack pair correlation function

In the formulation above, the inter-stack potential energy and pair correlation function are divided into four parts corresponding to the four types of stack pairs (Fig. 7). The first and the third parts deals with almost codirectional stacks. The second part deals with stacks at a relatively small angle. The fourth part deals with stacks that are randomly oriented relative to each other.

As a first approximation, we apply the perturbation as if the particles are in the same direction for the first three parts, and assume that the perturbation act on the average center-of-mass distance. For the first part, the perturbed distance between two stacks in direction  $\mathbf{u}_i$  can be estimated with a relation similar to Eq. (65):

$$\bar{r}_{1i}(\mathbf{F}) = \frac{\bar{r}_{1iR}}{|\mathbf{F}^{-T}\mathbf{u}_i|} = \frac{\exp(\mu_{1iR} + 5\sigma_{1iR}^2/2)}{|\mathbf{F}^{-T}\mathbf{u}_i|} = \exp(\mu_1(\mathbf{F}) + 5\sigma_1(\mathbf{F})^2/2) \quad (68)$$

Since we are considering a small perturbation, the number of pairs of stacks is considered unchanged, such that:

$$4\pi \rho_{\text{stackR}} N_{\text{stack}} \int g_{1R}(r) r^2 dr = 4\pi \rho_{\text{stack}}(\mathbf{F}) N_{\text{stack}} \int g_1(r) r^2 dr \quad (69)$$

$$J \exp(2\mu_{1iR} + 2\sigma_{1iR}^2/2) = \exp(2\mu_1(\mathbf{F}) + 2\sigma_1(\mathbf{F})^2/2) \quad (70)$$

together with Eq. (68), we then have the transformation rule for  $\mu_1$  and  $\sigma_1$ :

$$\mu_{1I}(\mathbf{F}) = \mu_{1R} + \frac{1}{3} \ln (|\mathbf{F}^{-T} \mathbf{u}_I|^2 J) \quad (71)$$

$$\sigma_{1I}(\mathbf{F}) = \sqrt{\sigma_{1R}^2 - \frac{1}{3} \ln (|\mathbf{F}^{-T} \mathbf{u}_I|^2 J)} \quad (72)$$

Similarly for the second part:

$$\mu_{2I}(\mathbf{F}) = \mu_{2R} + \frac{1}{3} \ln (|\mathbf{F}^{-T} \mathbf{u}_I|^2 J) \quad (73)$$

$$\sigma_{2I}(\mathbf{F}) = \sqrt{\sigma_{2R}^2 - \frac{1}{3} \ln (|\mathbf{F}^{-T} \mathbf{u}_I|^2 J)} \quad (74)$$

For the third part,  $\bar{r}_3$  and  $h$  are similarly transformed:

$$h_I(\mathbf{F}) = \frac{h_R}{|\mathbf{F}^{-T} \mathbf{u}_I|} \quad (75)$$

$$\bar{r}_{3I}(\mathbf{F}) = \sqrt{\frac{h_R^2}{4} |\mathbf{F} \mathbf{u}_I|^2 + \frac{r_{3R}^2}{2} (|\mathbf{F} \mathbf{u}_p|^2 + |\mathbf{F} \mathbf{u}_q|^2)} \quad (76)$$

The transform of  $g_4$  can be simplified into the transform of its argument  $r$ , due to its independence on orientation. For a set of vectors starting from one point with the same length  $r$ , the transformed vectors are in the form  $r\mathbf{F}\mathbf{t}$ , if we assume the unit vector is  $\mathbf{t}$ . We can calculate the root-mean-square length of the deformed vectors through the following integration:

$$r^2 = \frac{\int |r_R \mathbf{F} \mathbf{t}_R|^2 \sin \theta d\theta d\phi}{\int \sin \theta d\theta d\phi} \quad (77)$$

$$= \frac{r_R^2}{4\pi} \int \mathbf{F} \mathbf{t}_R \cdot \mathbf{F} \mathbf{t}_R \sin \theta d\theta d\phi \quad (78)$$

$$= \frac{r_R^2}{4\pi} \int \mathbf{t}_R \cdot \mathbf{C} \mathbf{t}_R \sin \theta d\theta d\phi \quad (79)$$

The variables  $\theta \in [0, \pi]$  and  $\phi \in [0, 2\pi]$  are the polar and azimuthal angles of the unit vector  $\mathbf{t}_R$ ;  $\mathbf{C} = \mathbf{F}^T \mathbf{F}$  is the right Cauchy–Green tensor. The unit vector can be given in terms of angles as  $\mathbf{t}_R = [\sin \theta \cos \phi, \sin \theta \sin \phi, \cos \theta]^T$ , with respect to the orthonormal basis that defines the spherical coordinates. The integration in Eq. (77) can be calculated:

$$r^2 = \frac{r_R^2}{3} \text{tr } \mathbf{C} \quad (80)$$

so that,

$$r(\mathbf{F}) = r_R \sqrt{\frac{1}{3} \text{tr } \mathbf{C}} = r_R \sqrt{\frac{1}{3} \mathbf{F} : \mathbf{F}} \quad (81)$$

The change in the inter-stack pair correlation function can be established through. :

$$4\pi \int g_{4R}(r_R) r_R^2 dr_R = 4\pi \int g_4\left(\frac{r}{\Gamma}\right) \frac{r^2}{\Gamma^3} dr = 4\pi \int g_4(r) r^2 dr \quad (82)$$

where  $\Gamma = \sqrt{(\mathbf{F} : \mathbf{F})/3}$ . Here  $\mathbf{F} : \mathbf{F} = F_{ij} F_{ij}$  is the inner product of the tensors, which is equal to the square of the norm of  $\mathbf{F}$ , i.e.  $\mathbf{F} : \mathbf{F} = |\mathbf{F}|^2$ . On the other hand, the right Cauchy–Green tensor is defined as  $\mathbf{C} = \mathbf{F}^T \mathbf{F}$ , so that  $\text{tr } \mathbf{C} = C_{ii} = F_{ij}^T F_{ji} = F_{ji} F_{ji} = \mathbf{F} : \mathbf{F}$ . The transformation rule for  $g(r)$  would be:

$$g_4(r) = \frac{1}{\Gamma^3} g_{4R}\left(\frac{r}{\Gamma}\right) \quad (83)$$

which, when reduced to the parameters of  $g_4$ , becomes:

$$\gamma_4(\mathbf{F}) = \frac{\gamma_{4R}}{\Gamma^3}, \quad \mu_4(\mathbf{F}) = \mu_{4R} + \ln \Gamma, \quad \sigma_4(\mathbf{F}) = \sigma_{4R} \quad (84)$$

### 3.3. Summary of elastic properties of mesoscale particle assembly

Compiling the results from the preceding sections we can now summarize the expressions for potential energy of the particle assembly;  $U(\Lambda, \mathbf{F}) = U_1(\Lambda, \mathbf{F}) + U_{21}(\Lambda, \mathbf{F}) + U_{22}(\Lambda, \mathbf{F}) + U_{23}(\Lambda, \mathbf{F}) + U_{24}(\Lambda, \mathbf{F})$ :

$$U_1(\Lambda, \mathbf{F}) = \sum_{l=1}^3 4\lambda_l \epsilon \epsilon_c N_{\text{stack}} \frac{a^2 + c^2}{2ac} (1.034\bar{m} - 1.070) \left[ \left( \frac{\sigma}{h_l(\mathbf{F})} \right)^{12} - \left( \frac{\sigma}{h_l(\mathbf{F})} \right)^6 \right] \left( 1 - \frac{2\delta_l(\mathbf{F})}{\pi a} \right)$$

$$U_{2I}(\Lambda, \mathbf{F}) = -2\pi \epsilon \rho_{\text{stack}}(\mathbf{F}) N_{\text{stack}}$$

$$\sum_{i=1}^3 \gamma_i \left[ \eta_1 \chi_1 \exp(2\mu_{ii}(\mathbf{F}) + 2\sigma_{ii}(\mathbf{F})^2) + c_\eta L \left( \frac{2\mu_{ii}(\mathbf{F}) - \ln v_\eta}{\sqrt{1 + \pi\sigma_{ii}(\mathbf{F})^2/2}} \right) + c_\chi L \left( \frac{2\mu_{ii}(\mathbf{F}) - \ln v_\chi}{\sqrt{1 + \pi\sigma_{ii}(\mathbf{F})^2/2}} \right) \right], \quad i = 1, 2$$

$$U_{23}(A, \mathbf{F}) = -2\pi\rho_{\text{stack}}(\mathbf{F})N_{\text{stack}}\gamma_3\epsilon_a(2\bar{m} - 1)\exp(2\mu_3 + 2\sigma_3^2) \frac{a^2 + c^2}{2ac}$$

$$\sum_{i=1}^3 \left( 1 + \frac{\sqrt{\epsilon_c} - \sqrt{\epsilon_a}}{2\sqrt{\epsilon_a}} \frac{h_i(\mathbf{F})^2}{2\bar{r}_{3i}(\mathbf{F})^2} \right)^2 u_{\text{LJ}}(\bar{r}_3(\mathbf{F}), h(\mathbf{F})/2)$$

$$U_{24}(A, \mathbf{F}) = \pi\epsilon\epsilon_a\rho_{\text{stack}}(\mathbf{F})N_{\text{stack}}\bar{m}^2 S^r(\mathbf{F})(S^{\parallel} + S^{\perp})$$

where the terms  $S^r(\mathbf{F})$  is given by:

$$S^r(\mathbf{F}) = 4\gamma_4(\mathbf{F})[\sigma^{12}\exp(-10\mu_4(\mathbf{F}) + 50\sigma_4(\mathbf{F})^2) - \sigma^6\exp(-4\mu_4(\mathbf{F}) + 8\sigma_4(\mathbf{F})^2)] \quad (85)$$

In principle, we are able to derive the analytical formulation of the components of the elasticity tensor through taking the derivative of the potential energy function  $U(A, \mathbf{F})$  with respect to the strain tensor  $\mathbf{E} = (\mathbf{F} + \mathbf{F}^T - \mathbf{1})/2$ . The analytical formulation however will be unnecessarily complicated to implement. Therefore in the actual calculation, the energy change can be numerically calculated corresponding to changes in different strain components. For example, in order to calculate  $C_{1112}$ , we start with infinitesimal strains:

$$\mathbf{E}^{(11)} = \begin{pmatrix} \epsilon & 0 & 0 \\ 0 & 0 & 0 \\ 0 & 0 & 0 \end{pmatrix}, \quad \mathbf{E}^{(12)} = \begin{pmatrix} 0 & \epsilon/2 & 0 \\ \epsilon/2 & 0 & 0 \\ 0 & 0 & 0 \end{pmatrix}, \quad \mathbf{E}^{(1112)} = \begin{pmatrix} \epsilon & \epsilon/2 & 0 \\ \epsilon/2 & 0 & 0 \\ 0 & 0 & 0 \end{pmatrix} \quad (86)$$

and calculate the corresponding small-deformation approximate deformation gradient associated with it:

$$\mathbf{F}^{(11)} = \begin{pmatrix} 1 + \epsilon & 0 & 0 \\ 0 & 1 & 0 \\ 0 & 0 & 1 \end{pmatrix}, \quad \mathbf{F}^{(12)} = \begin{pmatrix} 1 & \epsilon/2 & 0 \\ \epsilon/2 & 1 & 0 \\ 0 & 0 & 1 \end{pmatrix}, \quad \mathbf{F}^{(1112)} = \begin{pmatrix} 1 + \epsilon & \epsilon/2 & 0 \\ \epsilon/2 & 1 & 0 \\ 0 & 0 & 1 \end{pmatrix} \quad (87)$$

From these deformation gradients, the perturbed parameter set can be calculated and the perturbed potential energy can be estimated, denoted  $U^{(11)}$ ,  $U^{(12)}$ , and  $U^{(1112)}$ . If the potential energy of the unperturbed system is denoted  $U^{(0)}$ , the elasticity tensor component  $C_{1112}$  can be approximated as:

$$C_{1112} = \frac{1}{\epsilon V} \left( \frac{U^{(1112)} - U^{(12)}}{\epsilon} - \frac{U^{(11)} - U^{(0)}}{\epsilon} \right) = \frac{1}{\epsilon^2 V} (U^{(1112)} - U^{(12)} - U^{(11)} + U^{(0)}) \quad (88)$$

In general, if the perturbed strain magnitude in any mode is  $\epsilon$ , we have:

$$C_{ijkl} = \frac{1}{\epsilon^2 V} (U^{(ijkl)} - U^{(ij)} - U^{(kl)} + U^{(0)}) \quad (89)$$

### 3.3.1. Evaluation

With the potential energy known as a function of the mesostructure parameters, we can obtain the perturbed values of the parameters and calculate the potential energy changes as a result, from which the stiffness constants can be estimated with finite difference following the procedures provided in Section 3.2. Despite the overestimation of inter-stack potential energy described in Section 3.1.3, the model provides a reasonably good estimation of the elastic stiffness of the model. Table 2 summarizes the quantitative differences between the analytical and numerical stiffness results of the particle assemblies, in terms of the relative error between the orthotropically symmetrized version of the stiffness tensors. Here the relative errors are defined as:

$$\hat{\delta}_A^B = \frac{\|A - B\|}{\|B\|} \quad (90)$$

where  $\|\cdot\|$  is the Euclidean norm, i.e.,  $\|A\| = \sqrt{A : A}$ . The orthotropically symmetrized tensor  $\mathbb{C}^{\text{ortho}}$  has the following components in relation to the original tensor  $\mathbb{C}$ :

- $C_{iiii}^{\text{ortho}} = C_{iiii}$
- $C_{iijj}^{\text{ortho}} = (C_{iijj} + C_{jjii})/2$
- $C_{ijij}^{\text{ortho}} = C_{ijij} \quad (i \neq j)$
- All other terms are zero.

The theoretical model shows a low level of deviation from orthotropic symmetry ( $\hat{\delta}_{\text{th}}^{\text{th-ortho}}$ ). The relative error between the orthotropically symmetrized stiffness tensors from the numerical simulation and the analytical model estimation exhibit a deviation of around 12 to 30%. This however most likely due to the fact that the stack pair types we assumed in the model do not cover all pairs with a great accuracy, and that the model based on affine transformation that is applied to all particles may be too restrictive and can cause deviation from the real cases.

In order to provide a clearer perspective on the general trend of the elastic stiffness level with the confining pressure, we have used the following scalar measures:

**Table 2**

Relative error between the simulation results and theory prediction.

Pressure [Pa]	$\hat{\delta}_{\text{sim}}^{\text{sim-orth}}$	$\hat{\delta}_{\text{th}}^{\text{th-orth}}$	$\hat{\delta}_{\text{th-orth}}^{\text{sim-orth}}$
1	0.0168	0.0552	0.2041
5	0.0785	0.1136	0.2263
25	0.1582	0.0231	0.1192
125	0.2272	0.0456	0.3023

Notes: the relative error is defined as  $\hat{\delta}_A^B = \frac{\|A-B\|}{\|B\|}$ , where  $\|\cdot\|$  is the euclidean norm. The abbreviations are: sim = simulation, th = theory, orth = orthotropically symmetrized.

- $C_1 = (C_{1111} + C_{2222} + C_{3333})/3$  and  $C_2 = (C_{1122} + C_{2233} + C_{3311} + C_{2211} + C_{3322} + C_{1133})/6$  as average measures of the normal stress change in response to the normal strain.  $C_1$  is equivalent to an averaged value of the constrained moduli;
- $G = (C_{1212} + C_{1313} + C_{2323})/3$  as the average shear stiffness;
- $E = (S_{1111}^{-1} + S_{2222}^{-1} + S_{3333}^{-1})/3$  as the average Young's modulus.

where  $\mathbb{S} = \mathbb{C}^{-1}$  is the compliance tensor. Fig. 11-a compares the numerically computed stiffness measures  $C_1$ ,  $C_2$ ,  $G$ , and  $E$  with results of the proposed analytical model estimate. The theoretical estimation accurately simulates the general trend of the typical measures in response to the confining pressure, especially in the cases of average constrained modulus  $C_1$  and shear modulus  $G$ .

We have also carried out a preliminary comparison of the simulation results with existing (macroscopic/continuum level) experimental data, as shown in Fig. 11-b. Discrepancies are anticipated between the two sets of data. The experimental works are based on lab tests on reconstituted (BBC) and in-situ tests on two natural clays (Fucino and Izumo) that contain a wide range of particle sizes (silt and sands > 40%), and therefore can result in micro-structures at larger length scales, while the mesoscale numerical simulations are dealing with idealized systems comprising monodisperse illite particles. As a first order comparison, the results of mesoscale simulations were found to be at the same order of magnitude and follows similar power-law relations as the real data.

#### 4. Discussion and conclusions

This paper presented the establishment of a multiscale constitutive model for the small-strain elastic properties of assemblies of clay primary particles based on an analytical interpretation of mesoscale simulations (based on the computed interparticle forces and fabrics). The derivation of the model is based on the information provided by simulations at smaller length scales, and contains two parts: the homogenization schemes establishes the linkage between the mesostructure parameters and the potential energy of the system; and the perturbation scheme establishes the change of mesostructure parameters in response to small strains applied to the assemblies. The elastic stiffness of the systems, as a consequence, is calculated numerically as the second-order derivative of the potential energy with respect to the strain tensor.

In the evaluation of the model against the simulation results, we have found that the homogenization scheme of the model can capture accurately the intrastack potential energy but tends to underestimate the interstack potential energy. Elastic stiffness properties from the proposed perturbation scheme are within 12%–30% of those computed directly from numerical simulations. The analytical model also achieves very reasonable predictions of variations in stiffness with the level of confining stress. The overall trend in response to the variation of the confining pressure is very well captured. This is likely due to two factors:

- The division of potential energy according to the four representative types of stack pairs is not able to cover all stack pairs.
- The application of affine perturbations to every individual particle is not able to capture the real mechanism of elastic deformation.

However, as a first approximation, the model serves as a good starting point for further development.

In fact, the establishment of the multiscale model demonstrated the feasibility of building up macroscale/bulk properties of materials using a purely bottom-up approach, and fundamentally reflects the fact that the bulk properties of a material is solely determined by the interactions between the constituent units and the arrangement of these units. Although the model is established based on simulation of pure illite with similar setup as the numerical simulations, it can be applied to the study of real clay as well. The methodology also has the potential in the application to study multiscale features of engineering materials in general.

The proposed model has the potential of being developed into an elasto-plastic model through a combination of the current bottom-up approach and the top-down method through Coleman–Noll procedure (Coleman and Noll, 1963), analyzing the thermodynamics of the system using mesoscale structure parameters as internal variables. Specifically, the limitations in the current research that can be potentially developed and improved in future research include:

- Coarse-grained force field can incorporated hydration interaction and flexibility of particles;
- Explicit representation of water molecules in mesoscale simulation can be incorporated so as to study the drainage process in soils;
- Large deformation simulations can be carried out to study the change of mesostructure associated with plastic and failure behavior;
- The current model can be simplified through screening out the factors with negligible contributions.

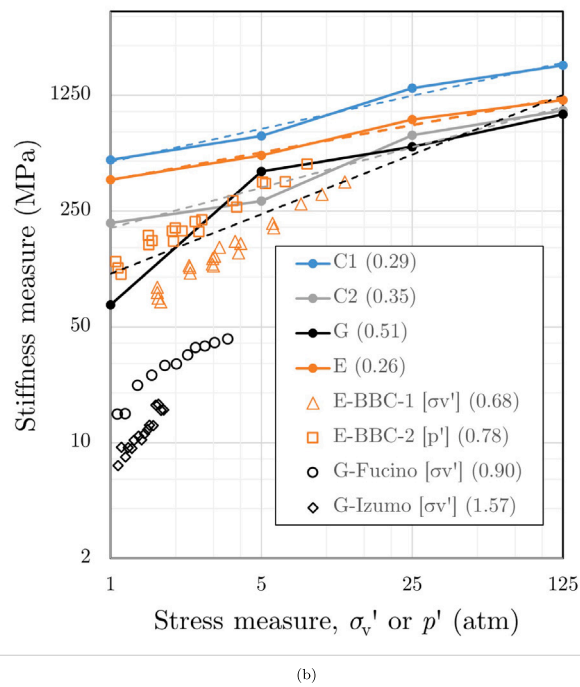
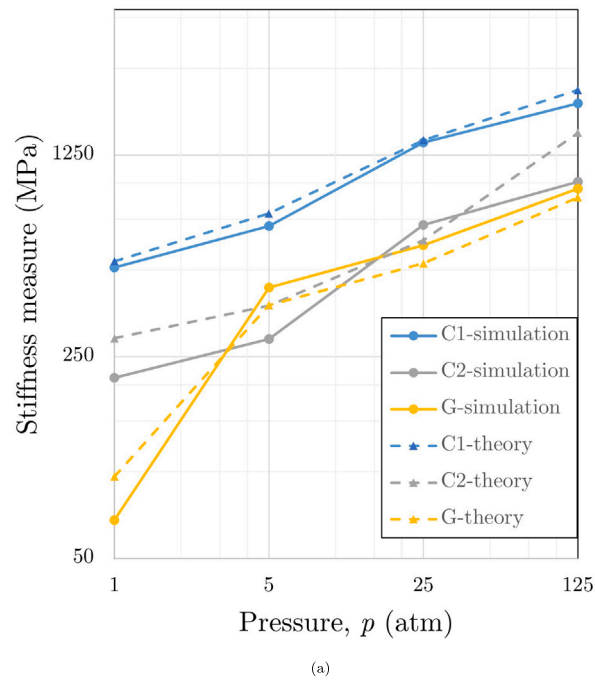


**Fig. 11.** Comparison between the evolution of stiffness measures of (a) simulation results and theoretical estimation; (b) simulation results and real data. Notes: All data points from the mesoscale simulations of this research study represent results averaged over 10 systems. In subfigure (b), bracketed value following the name of the stiffness measures are the exponent of power-law fits, following the relation  $Y = A\sigma^m$ , where  $Y$  is the measure ( $C$ ,  $G$ , etc.),  $\sigma$  is the stress measure and  $A, m$  are the fitting parameters. Simulated data use the mean stress  $p'$ . Experimental data represent 1D compression so that the vertical confining stress  $\sigma_v'$  is used, except E-BBC-2 where the stress measure was converted to mean stress  $p'$  by the author. The data are obtained from the following papers: G-Fucino and G-Izumo (Shibuya et al., 1997); E-BBC-1 (Santagata et al., 2007); E-BBC-2 (Santagata et al., 2005).

The upscaling methodology of this paper also has the potential of application in modeling other physical and chemical properties of materials in a broader context, and in the modeling of materials in other engineering disciplines.

### CRedit authorship contribution statement

**Hejian Zhu:** Writing – review & editing, Writing – original draft, Visualization, Validation, Methodology, Investigation, Formal analysis, Data curation, Conceptualization. **Andrew J. Whittle:** Writing – review & editing, Supervision, Resources, Project administration, Funding acquisition, Conceptualization. **Roland J.-M. Pellenq:** Writing – review & editing, Conceptualization.

### Declaration of competing interest

The authors declare that they have no known competing financial interests or personal relationships that could have appeared to influence the work reported in this paper.

### Acknowledgments

The Authors acknowledge the funding support from the US National Science Foundation (NSF) [ACI-1548562] under the grant no. 1702689 ‘Collaborative Research: Multi-scale Modelling and Measurement of Clay Aggregate Behaviour’. The first author also wants to acknowledge the help from Professor Lallit Anand, through insightful discussions during the establishment of the constitutive models. This work used the Extreme Science and Engineering Discovery Environment (XSEDE) (Towns et al., 2014) Stampede2 at Texas Advanced Computing Center (TACC) through allocations TG-MSS170021 and TG-MSS180023.

### Appendix A. Formulation of Gay–Berne potential for monodisperse axisymmetric particles

The current mesoscale analyses represent fundamental clay particles as single-site axisymmetric, ellipsoidal bodies using the Gay–Berne potential (Gay and Berne, 1981; Everaers and Ejtehadi, 2003). It is therefore possible to derive a simplified form of the Gay–Berne potential that describes the orientation of particles through unit normal vectors instead of rotation matrices or quaternions, enabling easier evaluation of the integration in the formulation. The derived form of the GB potential follows the earliest version derived by Gay and Berne (1981). This appendix gives another derivation in modern notations.

The most prevalent version of Gay–Berne potential contains three multiplicative components (Everaers and Ejtehadi, 2003):

$$U_{GB} = u_{LJ}\eta\chi \quad (\text{A.1})$$

where the components are calculated as:

$$u_{LJ} = 4\epsilon \left[ \left( \frac{\sigma}{r - \bar{\sigma} + \sigma} \right)^{12} - \left( \frac{\sigma}{r - \bar{\sigma} + \sigma} \right)^6 \right] \quad (\text{A.2})$$

$$\bar{\sigma} = \left( \frac{1}{2} \hat{\mathbf{r}}^T \mathbf{G}^{-1} \hat{\mathbf{r}} \right)^{-\frac{1}{2}}, \quad \hat{\mathbf{r}} = \frac{\mathbf{r}}{|\mathbf{r}|} \quad (\text{A.3})$$

$$\mathbf{G} = \mathbf{A}_1^T \mathbf{S}_1^2 \mathbf{A}_1 + \mathbf{A}_2^T \mathbf{S}_2^2 \mathbf{A}_2, \quad \mathbf{S}_i = \text{diag}(a_i, b_i, c_i), \quad i = 1, 2 \quad (\text{A.4})$$

$$\eta = \sqrt{\frac{2s_1 s_2}{\det(\mathbf{G})}}, \quad s_i = (a_i b_i + c_i c_i) \sqrt{a_i b_i}, \quad i = 1, 2 \quad (\text{A.5})$$

$$\chi = (2\hat{\mathbf{r}}^T \mathbf{B}^{-1} \hat{\mathbf{r}})^2 \quad (\text{A.6})$$

$$\mathbf{B} = \mathbf{A}_1^T \mathbf{E}_1 \mathbf{A}_1 + \mathbf{A}_2^T \mathbf{E}_2 \mathbf{A}_2, \quad \mathbf{E}_i = \text{diag}(\epsilon_{ia}^{-1/2}, \epsilon_{ib}^{-1/2}, \epsilon_{ic}^{-1/2}), \quad i = 1, 2 \quad (\text{A.7})$$

where  $r$  is the center-of-mass distance,  $\mathbf{A}_1$  and  $\mathbf{A}_2$  are the rotation matrices,  $\mathbf{S}_i$  and  $\mathbf{E}_i$  are the shape and energy matrices defining the shape of the ellipsoids and the relative depth of the potential wells. For clay particles in our simulations, the in-plane dimensions are the same, i.e.  $a_i = b_i$ , hence the shape matrix and the energy matrix are simplified as:

$$\mathbf{S} = \text{diag}(a, a, c), \quad \mathbf{E} = \text{diag}(\epsilon_a^{-1/2}, \epsilon_a^{-1/2}, \epsilon_c^{-1/2}) \quad (\text{A.8})$$

In the derivation of the simplified form of  $\mathbf{G}$  and  $\mathbf{B}$ , we start with the general additive term  $\mathbf{N} = \mathbf{A}^T \mathbf{M} \mathbf{A}$ , where  $\mathbf{M} = \text{diag}(\alpha, \alpha, \beta)$  and  $\mathbf{A}$  is the rotation matrix that transform from lab frame to local frame. Using the usual convention of Euler angles, where  $(\phi, \theta, \psi)$  are the precession, nutation and intrinsic rotation angles (Fig. A.12), we have the components of the rotation matrix:

$$\mathbf{A} = \begin{bmatrix} \cos \psi \cos \phi - \cos \theta \sin \phi \sin \psi & \cos \psi \sin \phi + \cos \theta \cos \phi \sin \psi & \sin \psi \sin \theta \\ -\sin \psi \cos \phi - \cos \theta \sin \phi \cos \psi & -\sin \psi \sin \phi + \cos \theta \cos \phi \cos \psi & \cos \psi \sin \theta \\ \sin \theta \sin \phi & -\sin \theta \cos \phi & \cos \theta \end{bmatrix} \quad (\text{A.9})$$

In the software LAMMPS, however, the orientation of the particles are represented by the quaternions. Quaternions are 3D generalization of the complex number. Unit quaternions are in one-to-one correspondence with rotation tensors. Each unit quaternion is composed of a vector in 3D space representing the rotation axis and a real number indicating the rotation angle, i.e.

$$\mathbf{q} = w + x\mathbf{i} + y\mathbf{j} + z\mathbf{k} = \cos \frac{\theta}{2} + \sin \frac{\theta}{2} (u_x \mathbf{i} + u_y \mathbf{j} + u_z \mathbf{k}) \quad (\text{A.10})$$

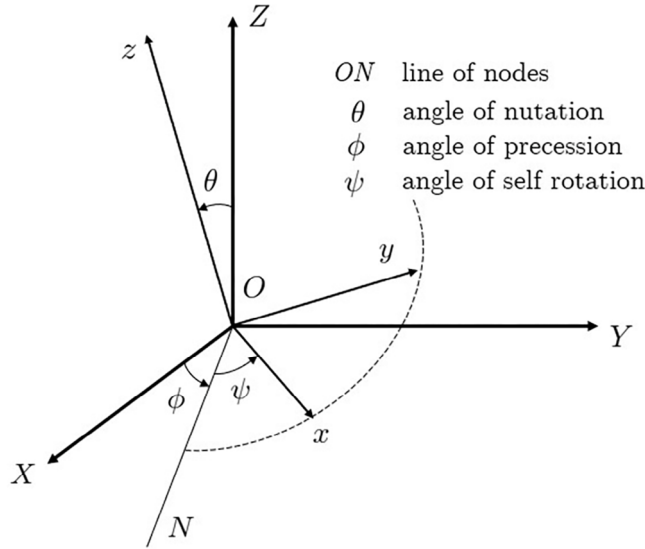


Fig. A.12. Schematic diagram of the  $zxz$ -convention of the Euler angles.

Notes: in the diagram, the global coordinate is represented by  $XYZ$  and local  $xyz$ , the translational displacement of the frame is omitted for clarity.

where  $\theta$  is the rotation angle, and  $(u_x, u_y, u_z)$  the components of the unit vector of the rotation axis (with  $u_x^2 + u_y^2 + u_z^2 = 1$ ). For a generic vector  $\mathbf{p} = (p_x, p_y, p_z)$ , which is in one-to-one correspondence with a quaternion  $\mathbf{p} = p_x \mathbf{i} + p_y \mathbf{j} + p_z \mathbf{k}$ , the resulting vector after the rotation is calculated through a conjugation operation  $\mathbf{p}' = \mathbf{q} \mathbf{p} \mathbf{q}^{-1}$ , where  $\mathbf{q}^{-1} = w - xi - yj - zk$  is the conjugate quaternion of  $\mathbf{q}$ . In the product, the components are calculated following the rules  $\mathbf{i}^2 = \mathbf{j}^2 = \mathbf{k}^2 = -1$  and  $\mathbf{i} \cdot \mathbf{j} = \mathbf{k} = -\mathbf{j} \cdot \mathbf{i}$ ,  $\mathbf{j} \cdot \mathbf{k} = \mathbf{i} = -\mathbf{k} \cdot \mathbf{j}$ ,  $\mathbf{k} \cdot \mathbf{i} = \mathbf{j} = -\mathbf{i} \cdot \mathbf{k}$ . The corresponding rotation tensor  $\mathbf{R}$  (such that  $\mathbf{p}' = \mathbf{R} \mathbf{p}$ ) can then be given by  $\mathbf{R} = \mathbf{v} \otimes \mathbf{v} + w^2 \mathbf{1} + 2w \mathbf{v} \times + (\mathbf{v} \times)^2$ , where  $\mathbf{v} = xi + yj + zk$ , and  $\mathbf{v} \times$  is the skew tensor corresponding to the vector  $\mathbf{v}$ . The components of the tensor  $\mathbf{v} \times$  is given by  $(\mathbf{v} \times)_{ij} = \epsilon_{ipj} v_p$ , where  $\epsilon$  is the Levi-Civita symbol, so that when applying the tensor to a generic vector  $\mathbf{n}$ , we have the relation  $(\mathbf{v} \times) \mathbf{n} = \mathbf{v} \times \mathbf{n}$ . In many texts, the vector  $\mathbf{v}$  is called the *axial vector* of the tensor  $\mathbf{v} \times$ , so that for a general skew tensor  $\Omega = \omega \times$ , its axial vector has the components  $\omega_i = \frac{1}{2} \epsilon_{piq} \Omega_{pq}$ . However in many other works, especially in the mathematics society (where axial vector is denoted  $\langle \Omega \rangle$ ), there is a sign convention difference, i.e.  $\langle \Omega \rangle_i = \frac{1}{2} \epsilon_{ipq} \Omega_{pq}$ . This definition has a convenient property in connection with the wedge product  $\mathbf{a} \wedge \mathbf{b} = \mathbf{a} \otimes \mathbf{b} - \mathbf{b} \otimes \mathbf{a}$  of two vectors  $\mathbf{a}$  and  $\mathbf{b}$ :  $\mathbf{a} \times \mathbf{b} = \langle \mathbf{a} \wedge \mathbf{b} \rangle$ . The tensor  $\mathbf{A}$  mentioned above is the inverse (or equivalently the transpose) of tensor  $\mathbf{R}$ . For the purpose of derivation here, we will stick to the Euler angle formulation given in Eq. (A.9). Following that, the components of  $\mathbf{N}$  could thus be calculated:

$$\mathbf{N} = \begin{bmatrix} \alpha - (\alpha - \beta) \sin^2 \theta \sin^2 \phi & (\alpha - \beta) \sin^2 \theta \sin \phi \cos \phi & -(\alpha - \beta) \sin \theta \cos \theta \sin \phi \\ \text{Sym} & \alpha - (\alpha - \beta) \sin^2 \theta \cos^2 \phi & (\alpha - \beta) \sin \theta \cos \theta \cos \phi \\ & & \alpha - (\alpha - \beta) \cos^2 \theta \end{bmatrix} \tag{A.11}$$

The components of the unit normal along the symmetric axis (assumed to be along the  $z$ -axis in local frame) is given by  $\mathbf{n} = [\sin \theta \sin \phi, -\sin \theta \cos \phi, \cos \theta]$  in the global coordinate system, which gives rise to a direct notation form of  $\mathbf{N}$ :

$$\mathbf{N} = \alpha \mathbf{1} - (\alpha - \beta) \mathbf{n} \otimes \mathbf{n} \tag{A.12}$$

Supposing the unit normals for the two interacting particles are  $\mathbf{n}_1$  and  $\mathbf{n}_2$ , and that the shape and energy matrices are the same for all particles (mono-dispersed system), we can specialize the form of  $\mathbf{G}$  and  $\mathbf{B}$  through Eq. (A.12). In the case of  $\mathbf{G}$ , we have  $\mathbf{M} = \mathbf{S}^2 = \text{diag}(a^2, a^2, c^2)$ , so that:

$$\mathbf{G} = 2a^2 \mathbf{1} - (a^2 - c^2)(\mathbf{n}_1 \otimes \mathbf{n}_1 + \mathbf{n}_2 \otimes \mathbf{n}_2) \tag{A.13}$$

Similarly,  $\mathbf{M} = \mathbf{E} = \text{diag}(\epsilon_a^{-1/2}, \epsilon_a^{-1/2}, \epsilon_c^{-1/2})$  implies:

$$\mathbf{B} = 2\epsilon_a^{-1/2} \mathbf{1} - (\epsilon_a^{-1/2} - \epsilon_c^{-1/2})(\mathbf{n}_1 \otimes \mathbf{n}_1 + \mathbf{n}_2 \otimes \mathbf{n}_2) \tag{A.14}$$

As expected, all these terms are only dependent on the unit normals instead of the rotation matrices. The form is in essence simplified through eliminating the angle of intrinsic rotation  $\psi$ .

Both tensors  $\mathbf{G}$  and  $\mathbf{B}$  share a common form, represented as  $\mathbf{P} = \mathbf{N}_1 + \mathbf{N}_2 = 2\alpha \mathbf{1} - (\alpha - \beta)(\mathbf{n}_1 \otimes \mathbf{n}_1 + \mathbf{n}_2 \otimes \mathbf{n}_2)$ . The GB formulation involves the calculation of the determinant of  $\mathbf{G}$  and the inverse of  $\mathbf{B}$ . The former can be derived with respect to a certain right-handed orthonormal basis  $\{\mathbf{e}_i\}_{i=1}^3$ :

$$\det \mathbf{P} \equiv \frac{\mathbf{P} \mathbf{e}_1 \cdot (\mathbf{P} \mathbf{e}_2 \times \mathbf{P} \mathbf{e}_3)}{\mathbf{e}_1 \cdot (\mathbf{e}_2 \times \mathbf{e}_3)} = \mathbf{P} \mathbf{e}_1 \cdot (\mathbf{P} \mathbf{e}_2 \times \mathbf{P} \mathbf{e}_3) = 8\alpha^2 \beta + 2\alpha(\alpha - \beta)^2 |\mathbf{n}_1 \times \mathbf{n}_2|^2 \tag{A.15}$$

Actually any right-handed set of independent vectors can be used. Here we use orthonormal basis for simplicity.

In the derivation of the inverse of  $\mathbf{P}$ , summation convention is not assumed. Since  $\mathbf{P}$  is a symmetric tensor, its inverse must also be symmetric. Therefore, together with the symmetry between  $\mathbf{n}_1$  and  $\mathbf{n}_2$ , we assume its inverse to be the most general form  $\mathbf{P}^{-1} = \mu \mathbf{1} + \nu(\mathbf{n}_1 \otimes \mathbf{n}_1 + \mathbf{n}_2 \otimes \mathbf{n}_2) + \Lambda(\mathbf{n}_1 \otimes \mathbf{n}_2 + \mathbf{n}_2 \otimes \mathbf{n}_1)$ , which indicates:

$$\begin{aligned} \mathbf{P}\mathbf{P}^{-1} &= \mathbf{1} = 2\alpha\mu\mathbf{1} + [2\alpha\nu - (\mu + \nu + \Lambda\mathbf{n}_1 \cdot \mathbf{n}_2)(\alpha - \beta)](\mathbf{n}_1 \otimes \mathbf{n}_1 + \mathbf{n}_2 \otimes \mathbf{n}_2) + \\ &\quad [2\alpha\Lambda - (\nu\mathbf{n}_1 \cdot \mathbf{n}_2 + \Lambda)(\alpha - \beta)](\mathbf{n}_1 \otimes \mathbf{n}_2 + \mathbf{n}_2 \otimes \mathbf{n}_1) \end{aligned} \quad (\text{A.16})$$

so that,

$$\mu = \frac{1}{2\alpha} \quad (\text{A.17})$$

$$\nu = \frac{\alpha^2 - \beta^2}{2\alpha[(\alpha + \beta)^2 - (\alpha - \beta)^2(\mathbf{n}_1 \cdot \mathbf{n}_2)^2]} \quad (\text{A.18})$$

$$\Lambda = \frac{(\alpha - \beta)^2(\mathbf{n}_1 \cdot \mathbf{n}_2)}{2\alpha[(\alpha + \beta)^2 - (\alpha - \beta)^2(\mathbf{n}_1 \cdot \mathbf{n}_2)^2]} \quad (\text{A.19})$$

with the help of these results, we can simplify  $\bar{\sigma}, \eta$  and  $\chi$  in the formulation given by Eq. (A.2).

$$\bar{\sigma} = 2a \left[ 1 + \frac{\omega_1[(\hat{\mathbf{f}} \cdot \mathbf{n}_1)^2 + (\hat{\mathbf{f}} \cdot \mathbf{n}_2)^2] + 2\omega_1^2(\mathbf{n}_1 \cdot \mathbf{n}_2)(\hat{\mathbf{f}} \cdot \mathbf{n}_1)(\hat{\mathbf{f}} \cdot \mathbf{n}_2)}{1 - \omega_1^2(\mathbf{n}_1 \cdot \mathbf{n}_2)^2} \right]^{-1/2} \quad (\text{A.20})$$

$$\eta = \sqrt{\frac{(a^2 + c^2)^2}{4a^2c^2 + (a^2 - c^2)^2|\mathbf{n}_1 \times \mathbf{n}_2|^2}} = [1 - \omega_1^2(\mathbf{n}_1 \cdot \mathbf{n}_2)^2]^{-1/2} \quad (\text{A.21})$$

$$\chi = \epsilon_a \left[ 1 + \frac{\omega_2[(\hat{\mathbf{f}} \cdot \mathbf{n}_1)^2 + (\hat{\mathbf{f}} \cdot \mathbf{n}_2)^2] + 2\omega_2^2(\mathbf{n}_1 \cdot \mathbf{n}_2)(\hat{\mathbf{f}} \cdot \mathbf{n}_1)(\hat{\mathbf{f}} \cdot \mathbf{n}_2)}{1 - \omega_2^2(\mathbf{n}_1 \cdot \mathbf{n}_2)^2} \right]^2 \quad (\text{A.22})$$

where

$$\omega_1 = \frac{a^2 - c^2}{a^2 + c^2} \quad (\text{A.23})$$

$$\omega_2 = \frac{\sqrt{\epsilon_c} - \sqrt{\epsilon_a}}{\sqrt{\epsilon_c} + \sqrt{\epsilon_a}} \quad (\text{A.24})$$

This result could be easily extended to dissimilar axisymmetric ellipsoidal particles. If the two particles have different  $\mathbf{S}$  and  $\mathbf{E}$  matrices:

$$\mathbf{S}_1 = \text{diag}(a_1, a_1, c_1), \mathbf{S}_2 = \text{diag}(a_2, a_2, c_2) \quad (\text{A.25})$$

$$\mathbf{E}_1 = \text{diag}(\epsilon_{a1}^{-1/2}, \epsilon_{a1}^{-1/2}, \epsilon_{c1}^{-1/2}), \mathbf{E}_2 = \text{diag}(\epsilon_{a2}^{-1/2}, \epsilon_{a2}^{-1/2}, \epsilon_{c2}^{-1/2}) \quad (\text{A.26})$$

the forms for  $\mathbf{G}$  and  $\mathbf{B}$  remain the same if we use  $\bar{a} = \sqrt{(a_1^2 + a_2^2)}/2$  and  $\bar{c} = \sqrt{(c_1^2 + c_2^2)}/2$  in place of  $a$  and  $c$ , and  $\bar{\epsilon}_a^{-1/2} = (\epsilon_{a1}^{-1/2} + \epsilon_{a2}^{-1/2})/2$  and  $\bar{\epsilon}_c^{-1/2} = (\epsilon_{c1}^{-1/2} + \epsilon_{c2}^{-1/2})/2$  in the place of  $\epsilon_a^{-1/2}$  and  $\epsilon_c^{-1/2}$  respectively. These changes can also propagate into the simplified forms of  $\bar{\sigma}$  and  $\chi$ , but for  $\eta$  as follows:

$$\eta = \sqrt{\frac{(a_1^2 + c_1^2)(a_2^2 + c_2^2)a_1a_2}{4\bar{a}^4\bar{c}^2 + \bar{a}^2(\bar{a}^2 - \bar{c}^2)^2|\mathbf{n}_1 \times \mathbf{n}_2|^2}} = \sqrt{\frac{(a_1^2 + c_1^2)(a_2^2 + c_2^2)a_1a_2}{4\bar{a}^4\bar{c}^2 + \bar{a}^2(\bar{a}^2 - \bar{c}^2)^2[1 - (\mathbf{n}_2 \cdot \mathbf{n}_2)^2]}} \quad (\text{A.27})$$

## Appendix B. Integration relations associated with lognormal functions

In the derivation of the potential energy (Section 3.1), the integration of the product of a rational function and a lognormal function is frequently used. This Appendix presents the derivation for the following two integrations:

$$I_1 = \int_0^\infty \frac{1}{\sigma\sqrt{2\pi x}} \frac{x^2}{x^2 + a} \exp\left(-\frac{(\ln x - \mu)^2}{2\sigma^2}\right) dx \quad (\text{B.1})$$

$$I_2 = \int_0^\infty \frac{1}{\sigma\sqrt{2\pi x}} x^2 \exp\left(-\frac{(\ln x - \mu)^2}{2\sigma^2}\right) dx \quad (\text{B.2})$$

The integrals revert to normal distribution forms through the change of variable  $t = \ln x$  ( $x \in [0, \infty)$ , so that  $t \in (-\infty, \infty)$ ):

$$I_1 = \int_{-\infty}^\infty \frac{e^{2t}}{e^{2t} + a} \mathcal{N}(t; \mu, \sigma) dt \quad (\text{B.3})$$

$$I_2 = \int_{-\infty}^\infty e^{2t} \mathcal{N}(t; \mu, \sigma) dt \quad (\text{B.4})$$

where  $\mathcal{N}(t; \mu, \sigma)$  is the normal distribution pdf with variable  $t$ , mean  $\mu$  and standard deviation  $\sigma$ , i.e.:

$$\mathcal{N}(t; \mu, \sigma) = \frac{1}{\sigma\sqrt{2\pi}} \exp\left(-\frac{(t - \mu)^2}{2\sigma^2}\right) \tag{B.5}$$

**Integration 1** With another change of variable  $q = 2t - \ln a$ ,  $I_1$  can be transformed in to the integration of the product of a unit logistic function and a normal distribution:

$$I_1 = \int_{-\infty}^{\infty} \frac{1}{1 + e^{-q}} \mathcal{N}(q; 2\mu - \ln a, 2\sigma) dq \tag{B.6}$$

For easier integration, the logistic function can be approximated by an normal cdf function (through setting their derivative at  $x = 0$  to be the same):

$$L(x) = \frac{1}{1 + \exp(-x)} \approx \int_{-\infty}^{\sqrt{\frac{\pi}{8}}x} \mathcal{N}(\Lambda; 0, 1) d\Lambda = \Psi\left(\sqrt{\frac{\pi}{8}}x\right) \tag{B.7}$$

The integration of the product of  $\Psi$  and  $\mathcal{N}$  can then be obtained as follows:

$$\int_{-\infty}^{\infty} \Psi(x) \mathcal{N}(x; m, s) dx = \int_{-\infty}^{\infty} \frac{1}{2} \left[ 1 + \operatorname{erf}\left(\frac{x}{\sqrt{2}}\right) \right] \mathcal{N}(x; m, s) dx \tag{B.8}$$

$$= \frac{1}{2} + \frac{\sqrt{2}}{2} \int_{-\infty}^{\infty} \operatorname{erf}(x') \mathcal{N}(x'; m/\sqrt{2}, s) dx' \tag{B.9}$$

$$= \frac{1}{2} + \frac{\sqrt{2}}{2} \frac{\sqrt{\pi}}{1/s} \operatorname{erf}\left(\frac{m/\sqrt{2}}{\sqrt{1+s^2}}\right) \frac{1}{s\sqrt{2\pi}} \tag{B.10}$$

$$= \frac{1}{2} \left[ 1 + \operatorname{erf}\left(\frac{m/\sqrt{2}}{\sqrt{1+s^2}}\right) \right] \tag{B.11}$$

$$= \Psi\left(\frac{m}{\sqrt{1+s^2}}\right) \tag{B.12}$$

so that,

$$\begin{aligned} \int_{-\infty}^{\infty} L(x) \mathcal{N}(x; \mu, \sigma) dx &\approx \int_{-\infty}^{\infty} \Psi\left(\sqrt{\frac{\pi}{8}}x\right) \mathcal{N}(x; \mu, \sigma) dx \\ &= \Psi\left(\frac{\sqrt{\pi/8}\mu}{\sqrt{1+\pi\sigma^2/8}}\right) \approx L\left(\frac{\mu}{\sqrt{1+\pi\sigma^2/8}}\right) \end{aligned} \tag{B.13}$$

The first integration can therefore be evaluated with the help of the above relations:

$$I_1 = \int_{-\infty}^{\infty} L(q) \mathcal{N}(q; 2\mu - \ln a, 2\sigma) dq \tag{B.14}$$

$$\approx L\left(\frac{2\mu - \ln a}{\sqrt{1+\pi\sigma^2/2}}\right) \tag{B.15}$$

$$= \left[ 1 + \exp\left(-\frac{2\mu - \ln a}{\sqrt{1+\pi\sigma^2/2}}\right) \right]^{-1} \tag{B.16}$$

**Integration 2** is actually simpler as the multiplication of  $\exp(2t)$  to the normal distribution causes merely a shift of the mean value:

$$I_2 = \int_{-\infty}^{\infty} e^{2t} \mathcal{N}(t; \mu, \sigma) dt \tag{B.17}$$

$$= \int_{-\infty}^{\infty} \mathcal{N}(t; \mu + 2\sigma^2, \sigma) \exp(2\mu + 2\sigma^2) dt \tag{B.18}$$

$$= \exp(2\mu + 2\sigma^2) \tag{B.19}$$

### Data availability

Data will be made available on request.

### References

Andrade, J., Avila, C., Hall, S., Lenoir, N., Viggiani, G., 2011. Multiscale modeling and characterization of granular matter: From grain kinematics to continuum mechanics. *J. Mech. Phys. Solids* 59 (2), 237–250. <http://dx.doi.org/10.1016/j.jmps.2010.10.009>.

- Asadi, F., Zhu, H.-X., Vandamme, M., Roux, J.-N., Brochard, L., 2022. A meso-scale model of clay matrix: the role of hydration transitions in geomechanical behavior. *Soft Matter* 18 (41), 7931–7948. <http://dx.doi.org/10.1039/D2SM00773H>.
- Bagi, K., 2006. Analysis of microstructural strain tensors for granular assemblies. *Int. J. Solids Struct.* 43 (10), 3166–3184. <http://dx.doi.org/10.1016/j.ijsolstr.2005.07.016>.
- Baumgarten, A.S., Kamrin, K., 2019. A general fluid-sediment mixture model and constitutive theory validated in many flow regimes. *J. Fluid Mech.* 861, 721–764. <http://dx.doi.org/10.1017/jfm.2018.914>.
- Brochard, L., 2021. Swelling of montmorillonite from molecular simulations: Hydration diagram and confined water properties. *J. Phys. Chem. C* 125 (28), 15527–15543. <http://dx.doi.org/10.1021/acs.jpcc.1c02659>.
- Brochard, L., Honório, T., Vandamme, M., Bornert, M., Peigney, M., 2017. Nanoscale origin of the thermo-mechanical behavior of clays. *Acta Geotech.* 12 (6), 1261–1279. <http://dx.doi.org/10.1007/s11440-017-0596-3>.
- Brochard, L., Vandamme, M., Pellenq, R.J., 2012. Poromechanics of microporous media. *J. Mech. Phys. Solids* 60 (4), 606–622. <http://dx.doi.org/10.1016/j.jmps.2012.01.001>.
- Carrier, B., 2014. Influence of Water on the Short-Term and Long-Term Mechanical Properties of Swelling Clays: Experiments on Self-Supporting Films and Molecular Simulations (Ph.D. thesis). Université Paris-Est.
- Chen, H., 2019. Constructing continuum-like measures based on a nonlocal lattice particle model: Deformation gradient, strain and stress tensors. *Int. J. Solids Struct.* 169, 177–186. <http://dx.doi.org/10.1016/j.ijsolstr.2019.04.014>.
- Chipot, A., Pohorille, A., 2017. *Free Energy Calculation*. Springer.
- Christoffersen, J., Mehrabadi, M.M., Nemat-Nasser, S., 1981. A micromechanical description of granular material behavior. *J. Appl. Mech.* 48 (2), 339–344. <http://dx.doi.org/10.1115/1.3157619>.
- Coleman, B.D., Noll, W., 1963. The thermodynamics of elastic materials with heat conduction and viscosity. *Arch. Ration. Mech. Anal.* 13, 167–178.
- Coussy, O., 2003. *Poromechanics*. John Wiley & Sons, Ltd.
- Coussy, O., 2007. Revisiting the constitutive equations of unsaturated porous solids using a Lagrangian saturation concept. *Int. J. Numer. Anal. Methods Geomech.* 31 (15), 1675–1694. <http://dx.doi.org/10.1002/nag.613>.
- Ebrahimi, D., Pellenq, R.J., Whittle, A.J., 2012. Nanoscale elastic properties of montmorillonite upon water adsorption. *Langmuir* 28 (49), 16855–16863. <http://dx.doi.org/10.1021/la302997g>.
- Ebrahimi, D., Whittle, A.J., Pellenq, R.J.-M., 2014. Mesoscale properties of clay aggregates from potential of mean force representation of interactions between nanoplatelets. *J. Chem. Phys.* 140 (15), 154309. <http://dx.doi.org/10.1063/1.4870932>.
- Everaers, R., Eftehadi, M.R., 2003. Interaction potentials for soft and hard ellipsoids. *Phys. Rev. E - Stat. Phys. Plasmas Fluids Relat. Interdiscip. Top.* 67 (4), 8. <http://dx.doi.org/10.1103/PhysRevE.67.041710>.
- Gay, J.G., Berne, B.J., 1981. Modification of the overlap potential to mimic a linear site-site potential. *J. Chem. Phys.* 74 (6), 3316–3319. <http://dx.doi.org/10.1063/1.441483>.
- Gens, A., Alonso, E.E., 1992. A framework for the behaviour of unsaturated expansive clays. *Can. Geotech. J.* 29 (6), 1013–1032. <http://dx.doi.org/10.1139/t92-120>.
- Gooneie, A., Schuschnigg, S., Holzer, C., 2017. A review of multiscale computational methods in polymeric materials. *Polymers* 9 (12), 16. <http://dx.doi.org/10.3390/polym9010016>.
- Gu, C., Kim, M., Anand, L., 2001. Constitutive equations for metal powders: application to powder forming processes. *Int. J. Plast.* 17 (2), 147–209. [http://dx.doi.org/10.1016/S0749-6419\(00\)00029-2](http://dx.doi.org/10.1016/S0749-6419(00)00029-2).
- Gurtin, M., Fried, E., Anand, L., 2010. *The Mechanics and Thermodynamics of Continua*. Cambridge University Press, URL <https://books.google.com/books?id=eGUQQaDsTsQC>.
- Heidug, W.K., Wong, S.-W., 1996. Hydration swelling of water-absorbent rocks: a constitutive model. *Int. J. Numer. Anal. Methods Geomech.* 20 (6), 403–430. [http://dx.doi.org/10.1002/\(SICI\)1096-9853\(199606\)20:6<403::AID-NAG832>3.0.CO;2-7](http://dx.doi.org/10.1002/(SICI)1096-9853(199606)20:6<403::AID-NAG832>3.0.CO;2-7).
- Holmboe, M., Wold, S., Jonsson, M., 2012. Porosity investigation of compacted bentonite using XRD profile modeling. *J. Contam. Hydrol.* 128 (1–4), 19–32. <http://dx.doi.org/10.1016/j.jconhyd.2011.10.005>.
- Honorio, T., Brochard, L., Vandamme, M., 2017. Hydration phase diagram of clay particles from molecular simulations. *Langmuir* 33 (44), 12766–12776. <http://dx.doi.org/10.1021/acs.langmuir.7b03198>.
- Horstemeyer, M., 2009. *Multiscale modeling: A review*. In: *Practical Aspects of Computational Chemistry*. Springer, pp. 87–135.
- Hueckel, T.A., 1992. Water-mineral interaction in hygromechanics of clays exposed to environmental loads: a mixture-theory approach. *Can. Geotech. J.* 29 (6), 1071–1086. <http://dx.doi.org/10.1139/t92-124>.
- Hueckel, T., 2005. Chemo-mechanics of geomaterials: Coupled constitutive laws. *Rev. Eur. Génie Civ.* 9 (5–6), 689–711. <http://dx.doi.org/10.1080/17747120.2005.9692777>.
- Kamrin, K., 2017. A hierarchy of granular continuum models: Why flowing grains are both simple and complex. In: Radjai, F., Nezamabadi, S., Luding, S., Delenne, J. (Eds.), *EPJ Web Conf.* 140, 01007. <http://dx.doi.org/10.1051/epjconf/201714001007>.
- Kamrin, K., 2018. Quantitative rheological model for granular materials: The importance of particle size. In: Andreoni, W., Yip, S. (Eds.), *Handbook of Materials Modeling*. Springer International Publishing, Cham, pp. 1–24.
- Karapiperis, K., Ortiz, M., Andrade, J., 2021. Data-driven nonlocal mechanics: Discovering the internal length scales of materials. *Comput. Methods Appl. Mech. Engrg.* 386, 114039. <http://dx.doi.org/10.1016/j.cma.2021.114039>.
- Kruyt, N., Rothenburg, L., 2004. Kinematic and static assumptions for homogenization in micromechanics of granular materials. *Mech. Mater.* 36 (12), 1157–1173. <http://dx.doi.org/10.1016/j.mechmat.2002.12.001>.
- Kuhn, M.R., 2005. Are granular materials simple? An experimental study of strain gradient effects and localization. *Mech. Mater.* 37 (5), 607–627. <http://dx.doi.org/10.1016/j.mechmat.2004.05.001>.
- Liu, L., 2002. *Continuum mechanics*. Advanced Texts in Physics, Springer Berlin Heidelberg, URL <https://books.google.com/books?id=gWqM4uMV6wC>.
- Mital, U., Andrade, J.E., 2022. Bridging length scales in granular materials using convolutional neural networks. *Comput. Part. Mech.* 9 (1), 221–235. <http://dx.doi.org/10.1007/s40571-021-00405-1>.
- Mitchell, J., Soga, K., 2005. *Fundamentals of Soil Behavior*, third ed. John Wiley & Sons, Ltd, Hoboken.
- Nejadsadeghi, N., Misra, A., 2020. Extended granular micromechanics approach: a micromorphic theory of degree n. *Math. Mech. Solids* 25 (2), 407–429. <http://dx.doi.org/10.1177/1081286519879479>.
- Placidi, L., Barchiesi, E., Misra, A., Timofeev, D., 2021. Micromechanics-based elasto-plastic damage energy formulation for strain gradient solids with granular microstructure. *Contin. Mech. Thermodyn.* 33 (5), 2213–2241. <http://dx.doi.org/10.1007/s00161-021-01023-1>.
- Santagata, M., Germaine, J.T., Ladd, C.C., 2005. Factors affecting the initial stiffness of cohesive soils. *J. Geotech. Geoenvironmental Eng.* 131 (4), 430–441.
- Santagata, M., Germaine, J.T., Ladd, C.C., 2007. Small-strain nonlinearity of normally consolidated clay. *J. Geotech. Geoenvironmental Eng.* 133 (1), 72–82.
- Shibuya, S., Hwang, S.C., Mitachi, T., 1997. Elastic shear modulus of soft clays from shear wave velocity measurement. *Géotech.* 47 (3), 593–601. <http://dx.doi.org/10.1680/geot.1997.47.3.593>.
- Towns, J., Cockerill, T., Dahan, M., Foster, I., Gaither, K., Grimshaw, A., Hazlewood, V., Lathrop, S., Lifka, D., Peterson, G.D., Roskies, R., Scott, J.R., Wilkins-Diehr, N., 2014. XSEDE: Accelerating scientific discovery. *Comput. Sci. Eng.* 16 (5), 62–74.
- Zhu, H., 2023. *Multiscale Modelling of the Mechanical Behavior of Clay* (Ph.D. thesis). Massachusetts Institute of Technology, Cambridge, MA.

- Zhu, H., Whittle, A.J., Pellenq, R.J.-M., 2022. Potential of mean force for Face2013Face interactions between pairs of 2:1 clay mineral platelets. *Langmuir* <http://dx.doi.org/10.1021/acs.langmuir.2c01632>, acs.langmuir.2c01632.
- Zhu, H., Whittle, A.J., Pellenq, R.J.-M., 2025. Mesoscale simulation of the compression and small-strain elastic shear behavior of illite nanoparticle assemblies. *Acta Geotech.* 20 (2), 781–802. <http://dx.doi.org/10.1007/s11440-024-02440-7>.
- Zhu, H.P., Yu, A.B., 2002. Averaging method of granular materials. *Phys. Rev. E* 66 (2), 021302. <http://dx.doi.org/10.1103/PhysRevE.66.021302>.
- Zwanzig, R.W., 1954. High-temperature equation of state by a perturbation method. I. nonpolar gases. *J. Chem. Phys.* 22 (8), 1420–1426. <http://dx.doi.org/10.1063/1.1740409>.